Effect of plasma hydrodynamics on laser-produced bremsstrahlung MeV photon dose

C. Courtois, A. Compant La Fontaine, T. Bonnet, F. Gobet, F. Hannachi, Jean-Raphaël Marquès, M. Tarisien, M. Versteegen, T. Vinci

Effect of plasma hydrodynamics on laser-produced Bremsstrahlung MeV photon dose

C. Courtois,[1] A. Compant La Fontaine,[1] T. Bonnet,[2] F. Gobet,[2] F. Hannachi,[2] J.R. Marquès,[3] M. Tarisien,[2] M. Versteegen[2], T. Vinci[3]

[1]CEA, DAM, DIF, F-91297 Arpajon, France
[2]Université de Bordeaux, Centre d'Etudes Nucléaires de Bordeaux Gradignan, UMR 5797 CNRS/IN2P3, Gradignan F-33175, France
[3]LULI, CNRS, CEA, Sorbonne Université, École Polytechnique, Institut Polytechnique de Paris, 91191 Gif sur Yvette, France

Corresponding author: Cedric Courtois, email: cedric.courtois@cea.fr.

We detail a laser plasma experiment aimed at enhancing laser to MeV electron energy coupling and then the x-ray dose produced when a short pulse laser propagates through a long preformed plasma. This study can be of interest for radiography of high areal mass objects requiring large doses but also for radiation safety of large scale laser facilities such as LMJ or NIF able to produce long preformed plasmas through which a short pulse laser can propagate. A low-intensity (~ 10^{14} W/cm^2) ns beam explodes a thin foil deposited on a high-Z solid target to generate an underdense plasma. An intense (> 10^{18} W/cm²) and short (< 1 ps) laser pulse then (with an adjustable delay δt) interacts with this plasma and produces multi-MeV electrons. These high-energy electrons are converted into a bremsstrahlung emission of MeV x-ray photons in the high Z target. In a second target design, a vacuum gap between the foil and the conversion target is also tested to let the plasma expand on both sides of the foil, increasing even more the interaction length. Results show how the vaporization of the foil produces an underdense plasma over several hundreds of micrometers which significantly enhances x-ray doses, with harder x-ray spectra obtained at an optimum delay, δt, until short pulse laser is affected by refraction. Increasing interaction length with gap targets is at the origin of a much more complex plasma hydrodynamics involving on-axis plasma stagnation which delays the optimum time for the maximum x-ray dose production.

I. INTRODUCTION

X-ray radiography is a powerful tool to probe internal features of objects. For most of the laser plasma experiments involving x-ray radiography of low or intermediate density objects, the photon energy used is within few keV to few tens of keV which is in the photoelectric absorption range.[1-3] X-ray radiography involving Compton scattering has already been reported.[4] Depending on the areal mass to probe, x-ray photon energy is then chosen to get contrasted radiography images. Radiographing high-Z and high areal mass object usually requires another approach. To maximize the object transmission, it is necessary to choose the photon energy that minimizes the object opacity. For tantalum for example, this is reached at Eγ ~4 MeV.[5] Then for a given photon energy, ideally centered at Eγ ~4 MeV for high-Z object, image signal to noise ratio is enhanced by increasing the number of x-ray photons produced to compensate low object transmission. The total attenuation coefficient (opacity) of 4MeV photons in a tantalum object of 100 g/cm² areal mass is around 4×10^{-2} cm²/g , showing that a transmission as low as 2% is indeed expected.

Laser Driven Radiography (LDR) has been studied for years and presents several advantages. Using for instance picosecond laser pulses, the ability to focus them on micrometer focal spots gives access to high temporal and spatial resolutions compared to more conventional devices based on electron induction accelerators, diodes or rod pinches used for the flash radiography.[6] The interaction of an intense (> 10^{18} W/cm²) laser pulse with a solid target generates multi-MeV relativistic electrons produced by different physical processes,[7] such as ponderomotive j×B acceleration,[8,9] direct laser acceleration,[10,11] wakefield acceleration.[12,13] Similarly to flash radiography machine, a high-Z solid target positioned behind the interaction area, converts high-energy electrons into MeV bremsstrahlung photons.[14,15] The objective of the present study is to increase x-ray dose from enhanced laser MeV electron energy coupling obtained by lengthening the interaction distance of the short pulse using long preformed plasmas. Achieving this can then be of interest to radiograph high areal mass objects,[16] it also contributes to enlarge the radiation safety database, to improve the ability

to do reliable predictions of dose on large scale laser facilities such as LMJ and NIF.[17] These facilities can indeed produce large scale plasmas through which intense short laser annexes pulses such as PETAL and ARC can propagate and deposit energy leading to the generation of energetic radiation.

The x-ray dose mainly depends on the intensity and energy of the short pulse laser, and the plasma parameters that govern the laser energy transfer into high energy electrons.[18-20] This paper presents an experimental study on the effects of large plasma scale lengths produced in front of a conversion target, on the properties of a bremsstrahlung x-ray source. In a previous similar study on the Alisé laser facility [21], plasma scale length up to L_p = 60 µm were tested. Results showed that MeV x-ray photon dose increases with the plasma size. Numerical simulations explain this by an increase of the laser energy absorption by hot electrons and an increase of the average kinetic energy of the accelerated electrons. In this present paper, the effects of larger plasma scale lengths, up to L_p = 500 µm, are presented. Two setups were tested. In the first one, the preformed plasma is produced by ionizing a polyethylene terephthalate plastic (PET) coated high Z (Ta) target with a ns laser beam focused on it before (a certain delay, δt) the short pulse arrival. The plastic coating is used to get a fast expanding preformed low Z plasma through which the short pulse laser propagates and converts its energy to MeV electrons. In the second one, the exploded PET foil is separated from the solid target by a vacuum gap (g) up to 700 µm wide. This increases the length of the preformed plasma by allowing it expanding from both sides of the foil. Reference shots were also performed without the ns laser pulse in which a lower x-ray dose is obtained.

The remainder of this paper is organized as follows. The experimental setup is described in Sec. II and experimental results in Sec. III. In Sec. IV, a bremsstrahlung dose analytical model coupled to 2D hydrodynamic simulations and benchmarked to PIC simulations is recalled and results from simulations are presented. Section V presents a comparison between experimental results and results from the dose model for different delays δt and gap distances g. An optimization of dose

production obtained by adjusting the ns long pulse focal spot size ϕ_{lp} is also discussed before the conclusion in Sec. VI.

II. EXPERIMENTAL SETUP

The setup of the experiment performed at the ELFIE facility at LULI, École Polytechnique, is represented in Fig.1(a). It uses three laser beams: a long pulse to create a preformed plasma, a short pulse that propagates through this plasma and produces energetic electrons, and a short probe laser to measure the plasma density. The long pulse (40 J/0.6 ns, wavelength $\lambda_0 = 1057$ nm) is focused on target with an incidence angle of 35° using a 1.1 m focal length lens and ablates a 1 µm thick polyethylene terephthalate plastic (PET) foil to generate the preformed plasma. The PET foil has no thin metal coating on it to block the long pulse rising edge that may go through it before foil ionization. The focal spot diameter is ϕ_{lp} = 160±20 µm full width at half maximum (FWHM) corresponding to a maximum laser intensity of ~ 1.6×10^{14} W/cm^2. The short pulse (E_{laser} = 7 J, Δt_{FWHM} = 0.4 ps, wavelength λ_0= 1057 nm, polarization p) is focused on target with an incidence angle of 10° in a FWHM spot size $\phi_0 = 10$ µm with an f/3 off-axis parabolic mirror (Rayleigh length Z_R ~ 300 µm). The laser radial intensity profile is Gaussian-like with an on-target peak intensity of I_0 = 4±2×10^{18} W/cm^2. The level of laser contrast due to the ASE (Amplified Spontaneous Emission) is around few 10^{-7} over 1 ns. When the ns pulse is not used, laser pedestal produces a preformed plasma of characteristic length L_p = 7 µm when the short pulse laser interacts with the target [see Fig. 4(a)]. When the long pulse is on, this pedestal has no effect on the foil hydrodynamics since the corresponding laser intensity, around 1×10^{12} W/cm², is low compared to 1.6×10^{14} W/cm^2. A probe beam (Δt_{FWHM} = 0.4 ps, wavelength λ = 528 nm) propagates parallel to the target surface. It is used to determine the preformed plasma electron density profile using an optical Nomarski interferometer.[22] The interferometer sensitivity and the refraction of the probe beam limit the plasma density measurement in the domain between ~ 10^{18} to ~ 5×10^{19} electrons/cm^3. During the experiment, the

delay δt between the long pulse and the short pulse is modified to study the variation of the bremsstrahlung x-ray emission for different gap values g. In the following, the time origin is defined at the long pulse maximum power and the short pulse is synchronized with this maximum for a delay δt = 0 ns [see Fig. 1(b)]. Note that all shots combining the long and the short laser pulses were performed with $\delta t \geq 0$ (delays up to 4 ns were investigated). A few reference shots were also performed with the short pulse only, without the plasma-preforming beam. These shots are assigned by convention to a negative delay of δt = -1 ns in the figures of this article. The probe pulse is synchronized to the short pulse.

The PET foil is separated by an empty gap from the front side of the 3 mm thick Ta solid metallic target [see Fig. 1(c)]. Different gaps were tested, g = 700 µm, g = 400 µm, g = 100 µm and g = 0 µm when the PET foil is directly coated on the Ta target. In this article, the origin of the z axis, along the PET foil normal, corresponds to the initial foil position [see Fig. 1(c)]. Positive values of z are associated to the region on the backside of the PET foil and negative values to the region on the frontside of the foil irradiated by the laser beams. The Ta target seen from the top exhibits a trapezoidal shape. The width of the foil mounted on the smaller length of the trapeze is 1 mm. This shape was chosen to limit laser probe diffraction on the left side of the foil (negative value of z) due to the Ta target edge.

Activation measurements and hard x-ray spectrometry,[23] are performed to determine the x-ray energy spectrum. The high energy part of the spectrum (> 10 MeV) is obtained by measuring photonuclear activation in copper and carbon samples at different angles behind the Ta target. These samples undergo (γ,n) photo-nuclear reactions such as $^{63}Cu(\gamma,n)^{62}Cu$ and ^{12}C $(\gamma,n)^{11}C$ which have different energy thresholds, about 10 and 18.7 MeV respectively. Assuming the high energy part of dN_γ/dE_γ follows a Boltzmann distribution, $dN_\gamma/dE_\gamma = K_\gamma \exp(-E_\gamma/T_\gamma)$, the temperature T_γ is determined from the measured ratio of the ^{62}Cu and ^{11}C activities and the amplitude K_γ from the absolute activities measurements.[24] The activation measurement gives information on the high energy part

(>10 MeV) of the x-ray spectrum. Note that the activation measurement is performed at different angles around the x-ray source. Since we only focus on the x-ray dose produced along the hard x-ray spectrometer axis described in the following paragraph, only measured activities along this axis are used to reconstruct x-ray spectra.

In addition to the activation technique, the low energy part (~MeV) of the photon spectrum is measured at a 12° angle relative to the z axis on the backside of the Ta target with a hard x-ray spectrometer. This spectrometer uses Fuji BAS-MS Imaging Plates (IPs) sandwiched between mm-scale tungsten filters housed inside a Denal (tungsten alloy) collimator.[25,26] The measurement is based on the absorption of photons by the tungsten filters. The absolute response of the stack of image plates has been calibrated with a ^{60}Co x-ray source at 1.25 MeV photon energy and simulated by Monte Carlo simulations. The analysis of the spectrometer results takes into account the x-ray absorption due to the Cu and C activation samples positioned around the target.

The x-ray photon energy spectrum dN_γ/dE_γ is then reconstructed consistently from both activation and absorption diagnostic measurements. Since low energy photons, typically below 0.5 MeV, are absorbed by the conversion target, the photon dose delivered in air at 1 m from the x-ray source is then computed from the reconstructed photon spectrum, considering a minimum photon energy $E_\gamma^{min} = 0.5$ MeV.

The x-ray source size was determined from a penumbral measurement using an 80 mm long, 4 mm inner diameter tantalum cylindrical pinhole drilled conically along its axis to create a circular absorbing edge. The size of the source is inferred by analyzing the edge of the penumbral image obtained on an image plate combined with Ta screens used to reinforce the signal strength relative to MeV photons.[24] Results are not presented in this paper that focuses on x-ray dose measurement. They show relatively small x-ray source size, within 100 µm to 200 µm, depending on the chosen delay δt and the gap value g, in spite of the use of thick mm scale Ta conversion target. This is explained by the fact that in a relativistic regime, the bremsstrahlung emission angle is relatively

narrow since it is proportional to $1/\gamma$, where γ is the Lorentz factor of the hot electrons. Since the x-ray source measurement is performed at an angle (<1°) close to the backlighter direction, only electrons propagating in this direction contribute to the signal on the detector. Since the electron scattering in a 3 mm thick Ta target is important, the x-ray source size, ϕ_x, is then mainly governed by the electron beam size, ϕ_e, on the Ta target and $\phi_x \sim \phi_e$. This explains the relatively small x-ray source size measured in this experiment and it also shows the interest of such laser produced source for x-ray radiography with high spatial resolution.

Finally, an electron spectrometer was used in a couple of shots for $\delta t = +0.5$ ns and without the Ta conversion target. Since no MeV photons are produced, activation measurement, the hard x-ray spectrometer and the penumbral aperture were removed from the experimental chamber for these particular shots. Electrons were deflected by a magnetic field produced by permanent magnets and recorded on imaging plates. The deflections of the electrons with their energy and the spectrometer sensitivity were calibrated. The minimum measurable electron energy is $E_e = 1.6$ MeV. The energy resolution is around ±0.08 MeV for $E_e = 2$ MeV, ±0.3 MeV for $E_e = 10$ MeV and ±3.5 MeV for $E_e = 40$ MeV.

III. EXPERIMENTAL RESULTS

Figure 2(a) represents the PSL signal level on 6 image plates (IP) of the hard x-ray spectrometer as a function of their position in the absorber sandwich, for two gap and delay combinations and when the long pulse is not activated ($\delta t = -1$ ns by convention). The image plate at position 1 is the least filtered and exhibits a stronger signal. Low x-ray signal is obtained on the first IP (~20 PSL/mm²) when the long pulse is off (and $g = 0$) and the signal amplitude is falling quickly with the IP position. When the long pulse is on, Fig. 2(a) shows a significant increase of the x-ray signal for $\delta t = 0.5$ ns and $g = 0$. The amplitude of the signal on the first IP is around 1000 PSL/mm²

and the signal is falling more slowly with the IP position. Note that at a later delay, $\delta t = 2$ ns and $g = 0$, the signal amplitude is still larger compared to the $\delta t = -1$ ns case, but it is lower compared to the $\delta t = 0.5$ ns case. The shot performed with a gap of $g = 400$ µm exhibits an even stronger signal on IP #1 (~2000 PSL/mm²) for a delay of $\delta t = 2$ ns which is as we will see the optimum delay that maximizes x-ray dose for that gap. These results show that first, producing a preformed plasma with a long pulse focused on target a certain delay prior the short pulse significantly increases the level of x-ray emission and second, that the optimum delay δt that maximizes the signal depends on the gap size. This means that the short pulse conditions of interaction quickly change with the hydrodynamics of the foil which depends on the gap value.

Figure 2(b) represents x-ray spectra inferred from results presented in Fig. 2(a) and activation measurements (the uncertainty is represented by the line thickness) for $g = 0$ and different delays and the corresponding cumulated dose in air at 1 m from the source. Fig. 2(b) shows as intuited by results from Fig. 2(a) that x-ray spectrum obtained with the short pulse only is very low compared to the case when the long pulse is combined to the short pulse laser. Adding this beam significantly increases the amplitude of the spectrum and also its temperature with much more multi-Mev photons produced. Note the significant effect of the delay δt on the spectra. For a delay $\delta t = 0.5$ ns, the cumulated dose is around 9 mrad (or 0.09 msieverts). For the shot performed without the long pulse, the x-ray dose is virtually zero. The x-ray dose is mainly carried here by photons of energy below 10 MeV.

Figure 2(c) represents similar results for a gap, $g = 400$ µm, with the same delays for comparison. The cumulated dose is shown for only one shot to keep the figure clear. Preforming a plasma with the long pulse increases again significantly the x-ray spectrum which is harder and exhibits a larger amplitude. Note that the maximum emission is obtained for another delay, $\delta t = 2$ ns (the corresponding cumulated dose is here around 15 mrad or 0.15 msieverts), which shows again that the conditions of interaction strongly depend on the gap.

The population of hot electrons at the origin of the bremsstrahlung x-ray emission was unfortunately not systematically measured during this experiment. A couple of spectra were obtained with the PET foil only, without the Ta target and for δt = + 0.5 ns. Fig. 2(d) is an example of spectrum showing that multi-MeV electrons are produced when the shot pulse propagates through the exploded PET foil. Multi-MeV electrons produce multi-MeV photons. As shown by Galy in reference [27], assuming the electron spectrum can be approximated by $\nu_0 E_e \exp(-E_e/T_e)$, where E_e is the electron energy and T_e the temperature characterizing the population of electrons and n0 the spectrum amplitude, a basic estimation of x-ray bremsstrahlung spectrum can be obtained after integrating the electron spectrum with the integrated-over-angle bremsstrahlung cross-section. It shows that the x-ray spectrum is proportional to $T_e \nu_0 Z^2 \exp(-E_\gamma/T_e)$, where E_γ is the photon energy. The temperature associated to the x-ray bremsstrahlung spectrum is then representative of the electron population temperature.

Figure 3 represents the x-ray dose in air at 1 m from the x-ray source inferred from the spectrometer and the activation measurements, normalized to the incident laser energy as a function of the delay δt and for different gaps. Dose is obtained after integration over the photon energy of the x-ray spectrum weighted by the air absorption coefficient which is relatively flat between 0.1 and 50 MeV.[5] X-ray dose is then a simple relevant quantity to consider comparing x-ray emission level between shots. For shots performed with the short pulse only (δt = -1 ns), the x-ray dose is very low, below 0.1 mrad (still measurable with the hard x-ray spectrometer). Preforming plasma prior to the short pulse arrival significantly increases x-ray emission. The maximum dose for the shots with no gap is obtained for δt = 0 ns. Shots performed with gap g = 100 µm show similar behavior but the maximum dose is obtained for a longer delay, δt = 1 ns. As the gap increases, the delay necessary to obtain the maximum dose also increases. For g = 400 µm and g = 700 µm, the maximum dose occurs at δt = 2 ns. Large x-ray doses are associated to harder x-ray spectrum [see Fig. 2].

Figure 4 shows examples of an interferogram of the expanding plasma obtained with the 2ω laser probe. Fig 4(a) is obtained when the long ns laser beam is not activated (g = 700 µm). The preformed plasma is produced by the short pulse laser ASE. The characteristic length of the plasma on the front side of the foil is short, around L_p = 7 µm. The image of Fig 4(b) is obtained when the long pulse is combined to the short pulse. The delay here is δt = 1 ns. At that time, plasma expansion can be seen on both sides of the PET foil and the expansion is much larger compared to the case when the long pulse is not activated. As a remainder, the PET foil has no thin metal coating on it to block the long pulse rising edge that may go through it before complete foil ionization. If transmitted laser energy occurs, it is should be limited since interferometry images (not presented here) show no associated plasma expansion from the Ta surface. A large portion of the long pulse energy seems then to be absorbed by the PET foil. Note that expanding plasma from the Ta surface could have been observed since the laser probe refraction would have bent 2ω laser probe photons trajectory toward negative values of z position, that is away from the large Ta target that can potentially clip laser probe.

Results presented on Fig. 3 show significant effects of the gap and the delay δt on x-ray emission. Since both parameters affect foil hydrodynamics, this is likely due to different conditions of interaction encountered by the short pulse laser during its propagation in the expanding underdense plasma. For non-zero gap, plasma can also expand at the rear side of the foil [see Fig. 4b)] and eventually collide with the Ta solid target at a time depending on the gap size. Thus it appears essential to perform 2D hydrodynamic simulations of the exploded foil to get a better understanding of these experimental results. X-ray measurements and hydrodynamic simulations are linked here via two approaches:

- 3D PIC CALDER[28] simulations coupled to Monte Carlo code MNCP,[29] but it can be limited by computing capability especially for long delay δt,
- a bremsstrahlung dose analytical model developed to overcome that aspect.

IV. MODEL AND NUMERICAL SIMULATIONS

Short pulse production of x-rays is usually performed in our simulations in three steps, with the 2D hydrodynamic radiative code TROLL,[30] the 3D PIC code CALDER,[28] and the Monte Carlo code MCNP,[29] which compute successively the preplasma density, the acceleration of electrons during the laser-plasma interaction, and electron propagation in the converter target, respectively. In this last step, collisions with atoms of the converter target and the bremsstrahlung process are simulated in particular. The maximum length of the plasma produced in this experiment is out of capability of the 3D PIC code CALDER. Intermediate sizes (L_p ~ 100 µm) require simulation times above 100 h with 1000 processors on the Tera1000 supercomputer at CEA-DIF. On a standard PC workstation, MCNP simulations for a thick Ta solid target typically require between a few tens to hundreds hours, depending on the nature of the element of the converter and on its thickness. Therefore, it appeared convenient to use an analytical model describing the bremsstrahlung dose to analyze experimental results and avoid such long simulations for each laser-target interaction condition. Complete numerical simulation, using CALDER, are achievable for the smallest plasma length, and for $\delta t = 0$.

A. HYDRODYNAMIC SIMULATION OF THE EXPLODED FOIL

Dynamics of the preformed plasma produced by exploding the foil with the long pulse is simulated using the 2D Lagrangian radiation-hydrodynamics code TROLL.[30] A 600 ps FWHM gaussian shape is used for the laser long pulse [see Fig. 1(b)] and simulations start 1 ns before the laser long pulse maximum (referenced as time). At that time, the laser intensity is low enough, around a few 10^{10} W/cm^2, so that plasma expansion can be neglected before that time. The PET foil is described along the z direction with 60 meshes constructed with a geometric progression for their size for a better description of the laser energy deposition inside the target. The size of this 2D cylindrical hydrodynamics simulation is 2 mm in length and 2 mm in radius (measured from the

simulation axis). Sesame EOS[31] and OPALV opacity[32] tables are used in the simulations. Electron thermal conduction was treated in the Spitzer-Harm formulation. The simulations were performed in the arbitrary lagrangian-eulerain (ALE) mode.

Figure 5(a) represents results of two numerical simulations. It shows a 2D-axisymmetric electron density n_e map at t = - 0.6 ns. The initial foil position is at z = 0 µm and the laser beams propagate from left to right. The top part of the image corresponds to a 400 µm gap and the lower part of the image to the second simulation performed with g = 0 µm. At that time, the plasma on the backside of the foil has not expanded yet and the density maps on the front side irradiated by the laser are virtually the same. Note the slight backward motion of the foil (z > 0) in the case of the 400 µm gap that does not exist with the zero gap since the Ta target prevents that back motion. For shots performed with a non-zero gap, the plasma from the exploded foil expands at the back side of the PET foil and eventually collides with the solid Ta target. Collision occurs at t_{coll} = 0.13 ns, t_{coll} = 0.58 ns and t_{coll} = 0.96 ns for g = 100 µm, g = 400 µm and g = 700 µm respectively.

Figures 5(b) and 5(c) represent a simulated 2D map of the electron density at t = + 0.5 ns (before collision) and t= + 1.8 ns (after collision) respectively, for the g = 700 µm gap. Plasma expansion is mainly longitudinal, that is along the z direction. Simulation results also show a transverse expansion of the plasma with radial velocity at the origin of on-axis material accumulation [see Fig. 5(c)]. Plasma longitudinal motion produces at first a hole in the PET foil and heated material from the edge of the hole subsequently expands radially towards the central axis. In this experiment, the duration of the long pulse is relatively short (0.6 ns FWHM) [see Fig. 1(b)], expanding plasma is then no longer heated after ~ t= + 1 ns and its pressure drops. The heated material from the edge is consequently no longer affected by the counter pressure produced by this plasma and it collides on axis. Thus inward motion is at the origin of material accumulation on axis that temporarily increases the electron density. Similar behavior can be observed in vacuum

hohlraum where laser ablated gold wall inward expansion also produces on-axis material accumulation.[33,34]

Figure 6 represents the on-axis (r = 0 µm) electron density n_e as a function of time for a 700 µm gap. The laser beam propagates from left to right and impacts the PET foil initially positioned at z = 0 µm. At early time, plasma expands mainly longitudinally from the front side of the exploded foil. Later on, plasma from the back surface of the foil becomes underdense relative to laser beams at around 0.45 ns before expanding then colliding Ta target at 0.96 ns. Plasma radial expansion shown on Fig. 5(c) is at the origin of an increase of density localized in time and space, around the initial position of the foil (z = 0 µm). It starts after t= + 1 ns and at t= + 1.8 ns the peak density at z = 0 µm is $n_e = 1.8\times10^{20}$ electrons/cm^3 and the FWHM of the density bump is 400 µm. Thus plasma radial expansion produces an underdense plasma of width comparable here with the Rayleigh length, Z_R, and of density above 10% of the critical density, n_{cr}. This increase of density is likely at the origin of the x-ray signal peak measured for the shots performed with a non-zero gap [see Fig. 3]. From Fig. 6, we would have also expected for g = 700 µm (but also for g = 400 µm and g = 100 µm) large x-ray dose produced for time between t = -1 ns and t = + 0.5 ns as short pulse laser also encounters high electron density during its propagation through the expanding plasma. As it will be shown in Sec. VA, energetic electrons produced by the short pulse laser in this preformed plasma are actually pulled back toward the PET foil because of strong electrostatic electric fields produced at the back of it, preventing electrons to collide with the Ta conversion target leading to x-ray dose reduction. This effect does not occur for g = 0 µm and a large dose is obtained at t = 0 ns for null gap target.

Results from simulated foil hydrodynamics have been compared to experiment. Figure 7(a) represents the simulated (gray region) on-axis (r = 0 µm) electron density profile at a later time, t= + 2 ns, for a zero gap case and the measured one inferred from the interferometry diagnostic (black dotted line). The upper and lower bounds of the gray region are associated to a ±10% variation on the long pulse energy during the TROLL simulations. Measured and simulated density profiles can

be approximated by an exponential decay characterized by a length L_p defined as, $n_e(z) = n_{Max}e^{-|z|/L_p}$. The maximum measured electron density accessible is 5×10^{19} e/cm^3 so that simulated electron density above this value can't be fully constrained by experimental data, especially for density close to the critical density the short pulse laser can potentially reach. Note that for the case, g > 0, as it will be shown later, measured maximum MeV x-ray dose is produced at late time (δt ~1-2 ns), in an underdense expending plasma of density around 1×10^{20} e/cm^3, which is not significantly above the maximum density accessible with the interferometry diagnostic. For g = 0, the maximum dose is obtained at t = 0 ns and the pulse laser interacts with a PET foil that has already expanded for 1 ns so it deposits its energy mainly in an underdense plasma of low density (few 10^{20} e/cm^3). The only case the short pulse laser can interact with electron density close to the critical density, inaccessible to the laser probe, is for delay δt ~ -1 ns when x-ray dose is very weak.

Figure 7(b) represents the simulated (gray region) and measured (symbols) characteristic length L_p as a function of time. A linear fit of the experimental data shows that the plasma from the front side of the foil is expanding with a velocity $V_f = 1.7\times10^7$ cm/s. Fig. 7(c) shows a similar figure but obtained in the case of a target with a gap g = 400 μm. As shown on Fig. 6 the foil hydrodynamics is affected by the plasma on-axis stagnation and thus more difficult to capture. Simulated L_p are within the errors bar of the measured L_p excepted at t = 1 ns. As shown on Fig. 6, that time corresponds to the moment when the expanding plasma collides with Ta and plasma density is low. Note that the collision time, t_{coll}, can't be obtained experimentally and then can't be compared to the simulated one to constraint more TROLL hydrodynamics simulations. The plasma expanding from the back side of the foil exhibits electron density gradients towards negative values of z position. Laser probe refraction in this plasma bends the 2ω probe photon trajectory toward positive values of z, that is toward the large Ta solid target that clips laser probe. The interferometry diagnostic can't then collect photons from the colliding region and the collision time can't be

inferred experimentally. Figure 7 shows that the foil expansion is relatively well captured by the 2D hydrodynamic simulation TROLL.

B. PIC NUMERICAL SIMULATION

The 3D PIC code CALDER[28] is used to simulate electron acceleration during the short pulse laser-plasma interaction. 3D simulations instead of 2D were performed because past studies showed that 2D simulations tend to underestimate the electron emission angle which in turn leads to an overestimation of the on-axis x-ray dose.[35] CALDER uses results from the TROLL simulation of the exploded PET foil as input data and more precisely the on-axis longitudinal plasma density n_e which depends on experimental conditions: the gap and the delay δt. The on-axis profile can be used here because the short pulse focal spot remains small compared to the transverse gradients of the expanding plasma. In the CALDER simulation, the short laser pulse is represented by Gaussian temporal and radial distributions with FWHM duration Δt_{FWHM} = 0.4 ps and spot size ϕ_{FWHM} = 10 µm, an energy E_{laser} = 2 J, and a maximum intensity $I_l = 0.42 \times 10^{19}$ W/cm^2. The contribution of the wings in the radial profile intensity to the production of the hot electrons is neglected here. The transverse width of the CALDER simulation box is 20 µm (the mesh size is $\lambda_0/20$) and the short pulse laser interacts with the underdense plasma at the plasma edge position associated to electron density larger than n_e/n_{cr} = 0.02 to shorten the length of the box and thus simulation time. Large plasma scale lengths produced in this experiment are out of capability of the 3D PIC code CALDER simulation, especially when a large gap is used since it potentially doubles the length of the simulation box. CALDER was then run in an intermediate size case, to simulate more precisely self-focusing effects when the short pulse propagates in the expanding plasma up to t= + 2 ns and only for cases without gap. Note that because of the moderated laser intensities considered and the low plasma electron density encountered by the short pulse laser, PIC simulations show that if self-focusing does occur, other laser propagation instabilities such as filamentation or bifurcation have

here moderated effect on on-axis x-ray dose production.[36,37] Results of CALDER simulations will be presented in the next part and used to benchmark the dose model.

C. BREMSSTRAHLUNG PHOTON DOSE ANALYTICAL MODEL

The bremsstrahlung dose model is described in detail in references [35], and later improved in reference [38] to take into account dose reduction due to electron return current in the conversion target. It assumes a nominal laser spot size ϕ_0 constant during the interaction of the ps pulse. Note that this model has already been compared successfully to experimental results in a previous paper,[20] where the x-ray dose was investigated for a fixed delay $\delta t = 0$ and a constant gap $g = 100$ µm, but varying the target element and thickness. Besides, the laser was focused on plasma with moderate scale length so that its density gradient was not considered in the interaction zone. In the study reported here, the high-energy electron converter is a tantalum target with a constant thickness of 3 mm and the laser produced x-ray source in the MeV photon range is optimized by changing the parameters δt and g from shot to shot to modify the conditions of interaction. The laser interacts with a plasma on a length of order or greater than the Rayleigh length, so that laser intensity varies significantly during the propagation, as well as the plasma density. These variations must therefore be taken into account, which is done in the present model. One can express the photon dose produced by hot electrons with mean kinetic energy $E_e(z)$ until position z in the plasma by:

$$D[E_e, z] \cong \frac{E_e(z) N_{el} \eta_{el}(z) R_E(X)}{2\pi(1-\cos\bar{\theta})d^2} \left(\frac{\mu_{en}}{\rho}\right)_{E_e}^{air} \sigma_r \rho \frac{N_A}{A} S e^{-\frac{X}{X_{ph}}} (1 - e^{-\frac{X}{S}}), \qquad (1)$$

The main process which produces x-ray emission in the MeV energy range is the bremsstrahlung radiation. Here, ρ in g/cm^3, A and X in cm correspond to the converter target density, its atomic mass and thickness respectively. N_A is the Avogadro number. $E_e(z) = \mu\, a_0(z)/\sqrt{2}$ is the kinetic energy of electrons expressed in MeV where $a_0(z) = 2.7\lambda_0\sqrt{I(z)/10^{19}}$ and I(z) expressed in W/cm² is the short pulse laser intensity at position z. It is assumed here that forward electrons are mainly produced

by the ponderomotive force of the laser. The function $\eta_{el}(z)$ is the fraction of the laser energy E_{laser} transferred to the hot electrons which brought the kinetic energy $E_e(z)$ from the initial position z = Z_{max} of the interaction, to the position z. The distance Z_{max} in cm is measured between the initial foil position (z = 0) and the position in the expanding plasma corresponding to the density $n_e = 2\times10^{19}$ electrons/cm^3 [see Fig. 8(a)]. As discussed in the previous section, this last position is constrained by the PIC simulation limited box size. This constraint is not an issue in this study as x-ray dose is mainly due to energetic electrons produced in plasma regions of density above 10^{20} electrons/cm^3 [see Fig. 11 for instance].

$$\eta_{el}(z) = \frac{1}{I_0 \Delta t}\int_{Z_{max}}^{z}\left(\frac{\phi(z)}{\phi o}\right)^2 n_e(z)E_e(z)dz. \qquad (2)$$

The distance $S = \left(X_{el}^{-1} - X_{ph}^{-1}\right)^{-1}$ is expressed in cm where X_{ph} is the photon mean free path and X_{el}, the hot-electron mean free path for ionization and bremsstrahlung. These two quantities are functions of $E_e(z)$. The bremsstrahlung dose model indicates that the photon mean free path can be interpolated here from NIST data[39] vs photon energy, E_γ, and expressed in cm by the following expression: $X_{ph}[E_\gamma] = [\rho(a_m E_\gamma^{bm} + 0.03\, E_\gamma^{-cm} + d_m)]^{-1}$, with $a_m = 0.0023Z^{-0.1}$, $b_m = 0.11Z^{0.46}$, $c_m = 0.29Z^{0.44}$, and $d_m = 0.0041Z^{0.5}$ with ρ given in gram per cubic centimeter and E_γ in mega-electron-volt, in the domain of validity: E_γ = {0.05, 100} MeV. The hot-electron mean free path X_{el} can be written $X_{el}(E_e) = [l_I^{-1}(E_e) + l_R^{-1}]^{-1}$ where $l_I(E_e)$ is its characteristic ionization length, and $l_R = 1/(n_a\sigma_r) = A/(\rho N_A\sigma_r)$ is the radiation length along with it loses 1/e of its energy by bremsstrahlung. The total bremsstrahlung cross section integrated over angles at high energy in the case of complete screening does not depend upon E_e and may be shown to be $\sigma_r = 4\bar{\sigma}[\ln(183Z^{-1/3}) + 1/18]$, with $\bar{\sigma} = Z(Z+1)r_e^2\alpha$ where r_e is the classical electron radius and α=1/137 is the fine structure constant so that l_R[cm] = 716.4A/{ρ[g/cm3]Z(Z+1)(ln(183Z$^{-1/3}$)+1/18)}. The characteristic ionization length is given by $l_I(E_e) = (1\text{-}e^{-5/3})E_e/F_I$ with $F_I[\mathrm{MeV/cm}] = 0.3070\frac{\rho[\mathrm{g/cm^3}]}{A}\frac{Z}{\beta^2}\ln\left(\frac{E_e\sqrt{\tau+2}}{I}\right)$, the force

produced by inelastic collision on the fast electrons, $\beta = \sqrt{1-(1+\tau)^{-2}}$ and $\tau = E_e/\mu$ with μ = 0.511 MeV. The mean excitation potential of elements with atomic number Z is noted I[eV] = 9.76Z + $5.58Z^{-0.19}$. The electron number is given by $N_{el} = E_{laser}/T_{h0}$, with $T_{h0} = \mu a_0/\sqrt{2}$. The function $(\mu_{en}/\rho)^{air}_{E_\gamma} = 0.01\left(1+1.5/\sqrt{E_\gamma}\right)$ describes the mass energy-absorption coefficient in air expressed in cm^2/g with energy given in MeV in the spectral range E_γ\{0.05, 100\} MeV. The quantity d in cm corresponds to the distance between the target and the plane where dose measurement is performed. X-ray dose in air is here defined at d = 100 cm from the source. The term R_E corresponds to the fraction of remaining electron kinetic energy at the end of the solid target of thickness X, resulting from the Ohmic heating energy loss process alone arising from the return current driven by the background electrons of the conductive target. Indeed, as the hot electrons cross the target, part of their energy is lost by Ohmic heating created by the electric field $\vec{E}$ set up by a return current $\vec{j}$, supplied by the thermal background electrons. This effect, which may inhibit the hot electron transport in conductive targets by increasing their energy loss leads to a reduction of the x-ray dose. For ELFIE experimental condition, $R_E(X)$~0.75. The angle $\bar{\theta}$ characterizes the mean opening angle of hot electron momentum direction. It writes $\bar{\theta}(\bar{E}_e, \bar{X}) \cong (\theta_0 - \theta_D)\exp(-\bar{X}/X_D) + \theta_D$, with $\bar{E_e} = R_E E_e$, $\bar{X} = S\ln\left[2/(1+\exp(-X/S))\right]$ and $\theta_0(E_e) = tg^{-1}\sqrt{2\mu/E_e}$ for L_p> 10 μm, and $\theta_0 \cong 2/\sqrt{\pi}$ for $L_p \le 10\,\mu m$. The angle $\theta_D = \cos^{-1}(1/e)$ is the Bethe's complete diffusion angle. In the ELFIE experimental conditions, the electron diffusion length X_D for tantalum averaged on the energy distribution of hot electrons is ~50 μm. The total dose is then obtained by the integration of Eq. (1) along the z axis. The expression of the x-ray dose normalized to the laser energy is derived from the fraction of energy absorbed by the hot electrons η_{el} and is given by the expression (3). The terms $\phi(z)$ and ϕ_0 in cm correspond to the laser focal spot diameter at the position z and at best focus in vacuum. The quantity n_e is on-axis (r = 0) electron density at the longitudinal position z. Note that in

Eq. (2), $n_e(z)$ instead of $n_e(z,r)$ is used for simplification since $\phi(z)$ remains relatively small between Z_{max} and z [see Fig. 8(a)], within ϕ_0, compared to the expanding plasma transverse gradients [see Fig. 5]. The total photon dose per laser energy unit produced by the hot electrons interacting in the plasma until position z_{abs} can thus be expressed by:

$$\frac{D}{E_{laser}}\left[\frac{mrad}{J}\right] \cong \frac{8.9\times10^{-21}R_E(X)}{(1-\cos\bar{\theta})d^2}\left(\frac{\mu_{en}}{\rho}\right)^{air}\sigma\rho\frac{Z(Z+1)}{A}\frac{1}{T_{h0}I_0\Delta t}\int_{z_{max}}^{z_{abs}}\left(\frac{\phi(z)}{\phi o}\right)^2 n_e(z)E_e^2(z)Se^{-\frac{X}{X_{ph}}}(1-e^{-\frac{X}{S}})dz\,, \quad (3)$$

The integration over z is performed up to the position z_{abs} defined as the point where laser energy is totally absorbed. Laser energy losses due to hot electrons energy gain are taken into account in our model coupled to TROLL simulations. Note that at early time, when plasma expansion is small enough so that laser energy is not totally absorbed, the integration over z is performed for electron density range n_e {0.02× n_{cr}, n_{cr}} where $n_{cr} \cong 1\times10^{21}$ electrons/cm^3 is the critical density at λ_0. The parameter Z corresponds to the atomic number of the target. The normalized total bremsstrahlung cross section integrated over angles and photon energy is written $\sigma=4[\ln(183Z^{-1/3})+1/18]$.

The laser beam diameter $\phi(z)$ considerably changes during laser focalization as does the hot electron kinetic energy $E_e(z)$. The short pulse focalization is first assumed to follow Gaussian beam law in the present photon dose model. Beam waist in vacuum then writes $w(z) = w_0\sqrt{1+(z/z_R)^2}$ where $Z_R = \pi W_0^2/\lambda_0 = 300$ µm is the Rayleigh length and $W_0 = \phi_0/(2\ln(2))^{1/2}$ is the waist. The short pulse laser is focused on the PET foil at the initial position z = 0. The gray solid line in Fig. 8(a) represents the evolution of w(z) using the above equation. Since the short pulse laser actually propagates in an expanding underdense plasma, the effect of laser self-focusing cannot be neglected. It is taken into account here by using a simplified parametrization of PIC CALDER simulation. The black solid line in Fig. 8(a) represents the simulated profile of electron density as a function of position z for the case without gap and δt = 0 ns. The simulation is performed using TROLL. The effect of short pulse self-focusing is represented by a simplified parametrization as a function of δt,

using two quantities, the waist W_{SF} and the focalization distance Z_{foc}, both defined on Fig. 8(a). This effect starts at the position z in the expanding plasma where $n_e = 2\times10^{19}$ electrons/cm^3 (position constrained by PIC simulation box size). The gray dotted line in Fig. 8(a) represents the evolution of w(z) including self-focusing effect inferred from CALDER PIC simulation. Taking into account this effect, the short pulse waist is modeled by the simple modified Gaussian beam equations:

$$w=W_{SF} \quad \text{for} \quad z>Z_{SF}, \quad \text{otherwise} \quad w(z) = W_{SF}\sqrt{1+\left[\frac{\lambda(Z_{foc}-z)}{\pi W_1^2}\right]^2} \quad \text{with} \quad W_1 = W_0\sqrt{\frac{\frac{Z_{foc}W_{SF}}{Z_R\ W_0}}{\sqrt{1+\left(\frac{Z_{max}}{Z_R}\right)^2-\left(\frac{W_{SF}}{W_0}\right)^2}}} \quad (4)$$

for z in the range $\{Z_{max},Z_{SF}\}$. Figures 8(b) and (c) represents W_{SF}/W_0 and Z_{foc} as a function a time determined from CALDER PIC simulations (black symbols). Figure 8(c) shows that at early time, W_{SF} is smaller than W_0 because of self-focusing effect. After t= + 0.5 ns, the short pulse propagates in large plasma and laser focalization is dominated by refraction effects that increase the focal spot size. As the delay δt increases, electron density gradients in the expanding plasma are getting smoother which consequently modifies the conditions of interaction of the short pulse laser and its propagation in the plasma underlined by the time evolution of Z_{foc} and W_{SF}/W_0. To determine ϕ(z) in the expression of the normalized dose, a link has to be estimated between W_{SF}/W_0, Z_{foc} and results from the hydrodynamic simulation of the exploded foil for the various gap values. It is assumed here that these two quantities are proportional to Z_{max} (that is to plasma expansion), with a condition on the ratio z/Z_R where Z_R is the short pulse Rayleigh length. Gray thick lines on Fig. 8(b) and (c) represent W_{SF}/W_0 and Z_{foc} as a function a time determined using the x-ray dose model in the case without gap, coupled to TROLL hydrodynamic simulations. The ratio W_{SF}/W_0 is set at 0.4 for $z/Z_R<1.2$ and to $W_{SF}/W_0=K_1\times Z_{max}$ for $z/Z_R>1.2$ with $K_1= 1.9\times10^{-3}$ µm^{-1}. The parameter $Z_{foc}=K_2\times Z_{max}$ is considered in the whole space with $K_2= 0.5$. Since Z_{max} is a function of the delay δt, so are these two parameters. The simple use of Z_{max} inferred from TROLL simulation to determine

the ratio W_{SF}/W_0 and Z_{foc} reproduces relatively well the time evolutions obtained from CALDER simulation in cases without gap. In this model, the description of laser self-focusing effect is simply sensitive to the expansion of the plasma in vacuum. In the following, it is assumed that the time evolution of W_{SF}/W_0 and Z_{foc} remains the same (proportional to Z_{max}) for gap values different from 0 for which limited PIC simulation capabilities prevent doing similar study. This is necessarily true at early time when plasma has not expanded yet on the backside of the foil (see for example Fig. 5(a) at t= - 0.6 ns). Later on, results from the model may be less quantitatively relevant.

V. COMPARISON BETWEEN MODEL AND EXPERIMENTAL RESULTS

This section presents comparisons between experimental results and the dose model for the different gaps tested. These comparisons are presented in a sequence of cases of increasing complexity. This approach involves no free parameters to constrain the model coupled to TROLL and CALDER simulations to experimental data (parameters W_{SF}/W_0 and Z_{foc} are for instance constrained by CALDER PIC simulation). TROLL and CALDER simulations are performed knowing the laser pulses parameters. The effect of uncertainties on PET foil thickness and long pulse energy on MeV x-ray dose is taken into account in this section.

A. Plasma sheath effect at the back of the foil at low value of the delay δt

Figure 9 shows the normalized x-ray dose as a function of the gap, for different times. The symbols correspond to the measurements obtained at δt = 0 ns (black triangles) and δt = 0.5 ns (open triangles). The x-ray emission decreases quickly with the gap. Because of computational time limitations, CALDER simulations were only performed for t= - 0.6 ns and gap values up to 200 µm. No comparison with experimental data can be done as the shortest delay tested experimentally with the long laser pulse is δt = 0 ns. Results of these calculations are reported in Fig. 9 as a thick line. The extrapolation of the CALDER results for gap values above 200 µm is constructed from the time

evolution of n_e at the backside of the foil determined from TROLL simulations. Note that at t= - 0.6 ns, the backside of foil has not expanded yet. Simulations show an even stronger decrease of the dose as a function of the gap than for delays δt = 0 and 0.5 ns. This is attributed to the electrostatic potential produced at the back of the target which pulls the hot electrons backwards to the target. As a consequence, the electron-photon conversion in the Ta target is strongly reduced.[40] The head of the population of hot electrons accelerated by the ponderomotive force are transmitted through the foil. Meanwhile, since ions have not moved yet, a Debye sheath forms at the back of the foil. The associated electric field that can reach several TV/m pulls the electrons back to the foil and only electrons with sufficient energy can escape the foil and impact the Ta converter.[40] Even if experimental and PIC results can't be directly compared, both show on Fig. 9 that as the gap increases, the number of electrons that reach the Ta target is reduced as is the x-ray dose. Simulated results also show that the effect of the sheath is even more important at early time when the sheath is still present and the associated x-ray dose is believed to be very weak (see gray thick curves of Fig. 11(a) and Fig. 12(a) at t = - 0.6 ns) and not measurable as it would require 10^4 measurement dynamics from Fig. 9. As time increases, the thin foil is ablated and expands towards the Ta target and the electrostatic sheath at the back of the foil weakens and has no longer an effect on the x-ray dose evolution.

The electrostatic sheath produced at the back of the PET foil lowers then here the x-ray emission as less electrons impact the Ta conversion target. Note that this is the opposite physics in the case of K-α x-ray emission source. These sources are usually based on thin foil, where electron refluxing due to electrostatic sheath increases x-ray emission. Preforming a plasma with a laser prepulse reduces on contrary the x-ray emission since the sheath is destroyed by the prepulse.[41] Fast electron escaping the target results then in less energy deposited back into the target. In our experiment, x-ray emission is affected on contrary at short time by electrostatic sheath effect at the backside of the foil that reduces the number of electrons transmitted by the PET foil, and later on by

the hydrodynamics of the foil, sensitive to gap thickness as it will be shown in Sec. VB and VC. In the following, the dose model corrected from the plasma sheath effect will be called "MODEL + TROLL + gap effect".

B. Effect of delay δt for the case without gap (g = 0)

Figure 10(a) presents the x-ray dose normalized to the laser energy as a function of delay and plasma scale length L_p. The plasma scale length is inferred from Fig. 7(b). The value of L_p for δt = -1 ns is determined from shots where the ns long pulse is not activated. Preformed plasma is then short and due to the short pulse ASE. Measured normalized dose from the ELFIE experiment, already presented on Fig. 3, is shown as the black triangles. The Alisé experiment mentioned in the introduction and performed with similar laser intensity allowed us to explore the effect of short plasma scale length (up to L_p = 60 µm) on x-ray dose. The Alisé experiment showed that longer plasma scale length increases laser energy absorption and electron kinetic energy. As shown by Eq. (2), the conversion efficiency, η_{el}, is sensitive to the short pulse laser propagation length and more precisely to the integration over this propagation distance of the product of the square of the short pulse focal spot size, the electron density and the electron energy. Assuming the forward electrons are mainly produced by the ponderomotive force of the laser, the electron energy is proportional to the laser vector potential, that is to the square root of the laser intensity. Thus the conversion efficiency is sensitive to the ability to propagate high intensity laser over long and dense plasma. It increases first with the size of the plasma until the plasma expansion is too important leading to laser refraction during the focusing stage which in return decreases the laser intensity and hot electrons energy. Since the short pulse laser power is much larger than the threshold power for relativistic self-focusing, the laser beam also self-focuses during its propagation in the preformed plasma. This produces higher laser intensities and then high electron kinetic energy and consequently larger x-ray emission.[42] Increasing the size of the preformed plasma also increases the length over which the short pulse laser can self-focus. Note also that for long preplasmas, laser absorption begins to take

place at high laser spot size, i.e. at low laser intensity, leading to total absorption of the laser energy before focusing, and to the production of lower-energy electrons and thus lower dose. This effect occurs because the laser energy available in the focal spot in the present study is only about 2 Joules. At higher laser energy, this effect would not take place. ELFIE experiment allows us to study x-ray dose evolution for larger length L_p. The dose is here maximum for L_p = 70 µm, then decreases. CALDER-MCNP simulations show a similar behavior but with a maximum dose for L_p ~ 30 µm. Results from the model [from Eq. (3)] indicate a maximum x-ray signal for L_p = 70 µm. The decrease of dose is due to short pulse laser refraction and to laser energy converted in low energy electrons useless for large MeV dose production. CALDER-MCNP and model results cannot be constrained by experimental data below 70 µm since no data was acquired between t= - 1 ns and t= 0 ns. Figures 10(b) to (d) show results from the model coupled to TROLL hydrodynamics simulations. Figure 10 (b) presents the on-axis (r = 0) plasma electron density as a function of position z and delay for n_e range $\{0.02\times n_{cr}, n_{cr}\}$. Only PET plasma is shown and not Ta for clarity. Plasma expansion from the front side of the foil is clearly visible. Figure 10 (c) presents the laser waist w(z) as a function of time using the model described in Sec. IVC [see Eq. (4)]. By definition, the position Z_{max} follows the position of the density $n_e = 2\times10^{19}$ electrons/cm^3 on Fig. 10 (b). The position z_{SF} where short pulse laser is self-focused to a spot size W_{SF} is also visible. According to the model, at t= 0 ns ($\delta t = 0$), the edge of the expanding plasma reaches the position $z = 1.2\times Z_R$ and laser beam starts to be affected by refraction. Its diameter increases and is even larger than W_0, the waist in vacuum, after t= + 0.35 ns [see Fig. 8(c)]. The evolution of w(z) with time can be directly seen on the evolution of the hot electron energy $E_e(z)$ [see Fig. 10 (d)]. For large value of $Z_{max} > Z_R$, low energy electrons useless for large MeV x-ray dose are produced. Electron energy is maximum for the z position up to z_{SF} where laser beam is self-focused and before t= 0 ns after which refraction affects laser propagation. The sharp evolution of w(z) and E_e at t~0 ns is due to the assumption made on the W_{SF}/W_0 evolution, set at 0.4 for $z/Z_R < 1.2$ and to $W_{SF}/W_0 = K_1\times Z_{max}$ for $z/Z_R > 1.2$. The x-ray dose

normalized to the laser energy, obtained from the model, as a function of delay is presented on Fig. 10 (a) (gray region). The x-ray dose first increases up to t = 0 ns since the self-focused short pulse laser propagates in the expanding plasma. The conversion efficiency, η_{el}, and the average kinetic energy of the accelerated electrons increase with L_p as discussed above. As the temperature associated to the x-ray bremsstrahlung spectrum is representative of the electron population temperature, harder x-ray and then electron spectra are then expected to be produced for increasing L_p up to 70 µm [see Fig. 2(b)]. Beyond that length, laser beam is affected by refraction that significantly increases the beam diameter which in return reduces the hot electron energy and the x-ray dose. Modifying the short pulse laser focusing point by a quantity Z_R ahead of the foil could reduce the refraction effect.

C. Delay time effects for the case GAP > 0

Figure 11(a) presents the x-ray dose normalized to the laser energy as a function of time for g = 400 µm. The measured dose from the ELFIE experiment, already presented on Fig. 3(a), is shown as black triangles. The x-ray dose increases with delay, is maximum at t= + 2 ns, then decreases. Figures 11 (b) to (d) show results from the model coupled to TROLL simulations (electron density, laser waist and hot electron energy respectively). At early time ($\delta t < 0$), plasma expansion is similar to the g = 0 µm case. Then the foil backside starts to slowly move and a plasma quickly expands before colliding with the Ta target at t_{coll} = 0.58 ns, which induces a more complex foil hydrodynamic evolution compared to the g = 0 µm case. The effect of the plasma radial expansion toward the foil axis (r = 0) already described in Sec. IVA is also visible. This inward expansion is at the origin of on-axis material accumulation which temporarily increases the electron density, here around the initial position of the foil (z = 0) between t= + 1 and t= + 2 ns. The gray region on Fig. 11 (a) corresponds to the x-ray dose normalized to the laser energy, obtained from the model, as a function of time. The dotted line corresponds to the normalized dose without taking into account its reduction due to the effect of the gap, that lowers the hot electrons flux transmitted to the target

because of the Debye sheath formed at the back of the foil [see Sec. VA]. By contrast to the case without gap [Fig. 10(a)], the dose shows two maxima, instead of one. This first maximum at about t= + 0.5 ns is produced when the plasma from the foil is getting undercritical relative to the short pulse laser. Laser beam can then propagate through both plasmas produced at the front and the back sides of the foil leading to a longer interaction length. Note that the first maximum at 0.5 ns occurs when the plasma reaches the Ta target, thus suppressing the reflection of the hot electrons by the plasma sheath. The x-ray dose then decreases after t= + 0.5 ns with the drop of on-axis electron density and increases because of on-axis material accumulation due to inward radial plasma collision. This drop could be related to the discrepancy between the measured and simulated characteristic length L_p [see Fig. 7(c)] observed at t = 1 ns. After that time (t= + 1.5 ns), the x-ray dose decreases with the electron density. The peak x-ray emission observed at t = + 1.5 ns is due to on-axis plasma stagnation (which does not occur for g = 0 µm) that produces a relatively dense (n_e~ 1×10^{20} e/cm^3) and long plasma produced at the front and the back sides of the initial foil position. This increases the interaction length of the short pulse laser and consequently produces larger conversion efficiency, η_{el}, and higher average electron kinetic energy as explained previously. Note that the decrease of x-ray dose after t = +1.5 ns, due to laser beam refraction that significantly increases the beam diameter which in return reduces the hot electron energy and the x-ray dose, seems to be less sharp compared to the case g = 0 µm. This could be explained by a weaker effect of laser refraction for g > 0 µm as preformed plasma is centred at the initial foil position (z = 0 µm) which also corresponds the short pulse focusing plane. For g = 0 µm, the preformed plasma is more centred towards negative values of z, that is toward the focusing region of the short pulse laser. The two peaks of dose are not observed experimentally possibly because of a too large delay between two laser shots. The assumed evolution of W_{SF}/W_0 and Z_{foc} and late time complex hydrodynamic simulations may also be likely less accurate than the gap g = 0 µm case. Yet, the simulated peak dose at t = + 1.5 ns is compatible with

the measured peak dose observed around t = + 1 ns and t = + 2 ns associated to harder electron and x-ray spectra [see Fig. 2(c)].

Results obtained with the larger 700 µm gap show similar behavior to the case with 400 µm gap. A maximum x-ray dose is also observed at t= + 2 ns due to material accumulation on axis which is independent of the gap size as long as it is large enough (400 µm and more in our case).

Figure 12(a) presents similar results as Fig. 10 and Fig. 11 for the case of a smaller gap: 100 µm. The measured dose is maximum at t= + 1 ns, which is between the large gap case (400 µm and above) [see Fig. (11)] and the case without gap [see Fig. 10]. Figure 12(b), shows that the on-axis (r = 0) plasma electron density evolution is different from the large gap case since no material accumulation is observed. The plasma expanding from the backside of the foil impacts the Ta solid target at t_{coll} = 0.13 ns, bounces on it, producing a forward perturbation that swipes the plasma produced at the front side of the foil. That phenomenon limits material accumulation and the associated peak of x-ray dose at t= + 2 ns observed for g = 400 µm and g = 700 µm does not exist here. The peak of dose at t= + 0.25 ns is not observed experimentally. Again, this may be due to a too large time increment between two shots missing the peak but also to the limit of numerical simulations to quantitatively capture the complex evolution of the exploded PET foil where longitudinal and radial plasma expansion occur on a same time scale as the plasma collision on solid Ta wall and the forward perturbation. The 100 µm gap case is therefore the most difficult one to apprehend in this study.

D. Dose optimization

Results presented in Sec. VC show that in the case of a gap large enough (≥ 400 µm here), the early longitudinal expansion of the plasma produces, a drop of electron density at the initial foil position on axis (r = 0). Yet plasma radial inward expansion is at the origin of an on-axis material accumulation that increases n_e locally in time and space (around z = 0 µm). In this experiment, the foil is exploded using a long pulse laser of focal spot diameter ϕ_{lp} = 160 µm. Working with a smaller

focal spot should increase the peak electron density since plasma propagates radially on a shorter distance, with less dilution, before on-axis collision. The time to reach the peak density is also expected to be shorter and should be compared to t_{coll} to make sure that the effect of the gap that lowers the hot electrons flux transmitted to the conversion target (because of the Debye sheath formed at the back of the foil [see Sec. VA]) is not limiting x-ray dose production. Figure 13 presents results from the dose model combined to TROLL hydrodynamic simulation and corrected from gap effect for a 400 µm gap. Figures 13(a) and (b) show the maximum normalized dose as a function of the long pulse focal spot diameter ϕ_{lp} and the time at which the maximum dose is produced respectively. Results are obtained at constant laser intensity. In the condition of the experiment (ϕ_{lp} = 160 µm), maximum dose is obtained at t= + 1.4 ns and reaches 2.1 mrad/J. Since that time is larger than t_{coll} = 0.58 ns, the Debye sheath formed at the back of the foil does not reduce the dose. Decreasing the focal spot diameter ϕ_{lp} increases the level of dose and reduces the time when maximum dose is produced. A maximum dose ~ 4.4 mrad/J is obtained for ϕ_{lp} = 95 µm which double the signal strength compared to experimental results. Below this value, dose production is affected by the effect of the Debye sheath and the x-ray dose decreases with ϕ_{lp}. This study assumes that results from Fig. 9 on gap effect obtained for ϕ_{lp} = 160 µm are still valid. Thus it was performed at constant laser intensity and not at constant laser energy to try to maintain a relatively similar foil dynamics if one excludes 2D effects.

VI. CONCLUSION

This study aimed at increasing x-ray dose of a MeV bremsstrahlung source created when an intense (> 10^{18} W/cm^2) and short pulse laser produces relativistic electrons that collide with a high-Z solid target. Electrons are generated in a large plasma created with a ns beam (focused before the short pulse with a delay δt), that explodes a thin PET foil positioned in the front of the solid target,

separated from it by a gap g. X-ray emission is optimized by changing from shot to shot the parameters δt and g to produce different plasma scale lengths L_p encountered by the short pulse laser.

Results from a dose model coupled to a 2D hydrodynamic code to simulate the preformed plasma time evolution and benchmarked at early time with PIC simulation results are compared to experimental data. They both show that for the simplest case considered hydrodynamically speaking, g = 0, x-ray dose is very weak when the short pulse laser is used alone so that it interacts with a small plasma (L_p = 7 µm) produced by the laser ASE. Adding a preformed plasma with the ns pulse significantly increases the x-ray dose, until L_p = 70 µm. This increase, due to a hardening of the x-ray spectra and larger spectrum amplitude, is explained by higher average kinetic energy of hot electrons and larger laser energy absorption. Beyond L_p = 70 µm, the laser beam starts to be affected by refraction and x-ray dose decreases.

Using targets with gap (g > 0) to increase the interaction length is at the origin of a much more complex plasma hydrodynamics involving on-axis plasma stagnation which delays the optimum time for maximum x-ray dose production and at early time, self-consistent electrostatic fields formed at the rear of the foil that reflect electrons backwards towards the foil limiting the x-ray emission. Maximum MeV x-ray dose, obtained at the optimum time function of the gap size, is also associated to a hardening of the electron and photon spectra for g > 0. The amplitude of this maximum seems however constant in our experimental conditions with and without gap and whatever its size. A possible explanation is that in our hydrodynamics regimes, short pulse laser energy is entirely absorbed by the expanding plasma at the time of maximum emission. A third parameter, the ns long beam focal spot size, is introduced to maximize the MeV x-ray dose for g > 0.

AKNOWLEDGMENTS

We acknowledge the technical support of the operations staff on ELFIE facility at LULI, École Polytechnique for the laser operation, and data acquisition, the target fabrication at CEA-Valduc and

the support system of the Tera1000 Bull supercomputer at CEA/DIF for providing the computing resources necessary to run the PIC simulations on multiparallel processors.

DATA AVAILABILITY

The data that support the findings of this study are available from the corresponding author upon reasonable request.

REFERENCES

[1]A. Ravasio, M. Koenig, S. Le Pape, A. Benuzzi-Mounaix, H. S. Park, C. Cecchetti, P. Patel, A. Schiavi, N. Ozaki, A. Mackinnon, B. Loupias, D. Batani, T. Boehly, M. Borghesi, R. Dezulian, E. Henry, M. Notley, S. Bandyopadhyay, R. Clarke, and T. Vinci1, Phys. Plasmas **15**, 060701 (2008).

[2]A. Morace, L. Fedeli, D. Batani, S. Baton, F. N. Beg, S. Hulin, L. C. Jarrott, A. Margarit, M. Nakai, M. Nakatsutsumi, P. Nicolai, N. Piovella, M. S. Wei, X. Vaisseau, L. Volpe, and J. J. Santos, Phys. Plasmas **21**, 102712 (2014).

[3]E. Brambrink, H. G. Wei, B. Barbrel, P. Audebert, A. Benuzzi-Mounaix, T. Boehly, T. Endo, C. Gregory, T. Kimura, R. Kodama, N. Ozaki, H.-S. Park, M. Rabec le Gloahec, and M. Koenig, Phys. Plasmas, **80**, 056407 (2009).

[4]R. Tommasini, S. P. Hatchett, D. S. Hey, C. Iglesias, N. Izumi, J. A. Koch, O. L. Landen, A. J. MacKinnon, C. Sorce, J. A. Delettrez, V. Yu. Glebov, T. C. Sangster, and C. Stoeckl, Phys. Plasmas, **18**, 056309 (2011).

[5]J M. Boone, A E. Chavez; Medical Physics **23**, 1997 (1996).

[6]T. J. Goldsack, T. F. Bryant, P. F. Beech, S. G. Clough, G. M. Cooper, R. Davitt, R. D. Edwards, N. Kenna, J. McLean, A. G. Pearce, M. J. Phillips, K. P. Pullinger, D. J. Short, M. A. Sinclair, K. J. Thomas, J. R. Threadgold, M. C. Williamson, and K. Krushelnick, IEEE Trans. Plasma Sci. 30, 239 (2002).

[7]M. I. K. Santala, M. Zepf, I. Watts, F. N. Beg, E. Clark, M. Tatarakis, K. Krushelnick, A. E. Dangor, T. McCanny, I. Spencer, R. P. Singhal, K. W. D. Ledingham, S. C. Wilks, A. C. Machacek, J. S. Wark, R. Allott, R. J. Clarke, and P. A. Norreys, Phys. Rev. Lett. **84**, 1459 (2000).

[8]G. Malka and J. Miquel, Phys. Rev. Lett. **77**, 75 (1996).

[9]S. C. Wilks, W. L. Kruer, M. Tabak, and A. B. Langdon, Phys. Rev. Lett. **69**, 1383 (1992).

[10]A. Pukhov, Report Progress in Physics **66**, 47 (2003).

[11]C. Gahn, GD. Tsakiris, A. Pukhov, J. Meyer-ter Vehn, G. Pretzler, P. Thirolf, D. Habs, and K.J. Witte, Phys. Rev. Lett. **83**, 4772 (1999).

[12]T. Tajima and J. M. Dawson, Phys. Rev. Lett. **43**, 267 (1979).

[13]F. Amiranoff, S. Baton, D. Bernard, B. Cros, D. Descamps, F. Dorchies, F. Jacquet, V. Malka, J. R. Marquès, G. Matthieussent, P. Miné, A. Modena, P. Mora, J. Morillo, and Z. Najmudin, Phys. Rev. Lett. **81**, 995 (1998).

[14]E. Lefebvre, N. Cochet, S. Fritzler, V. Malka, M. M. Aléonard, J. F. Chemin, S. Darbon, L. Disdier, J. Faure, A. Fedotoff, O. Landoas, G. Malka, V. Méot, P. Morel, M. Rabec Le Gloahec, A. Rouyer, C. Rubbelynck, V. Tikonchuk, P. Wrobel, P. Audebert, and C. Rousseaux, Nucl. Fusion **43**, 629 (2003).

[15]R. D. Edwards, M. A. Sinclair, T. J. Goldsack, K. Krushelnick, F. N. Beg, E. L. Clark, A. E. Dangor, Z. Najmudin, M. Tatarakis, B. Walton, M. Zepf, K. W. D. Ledingham, I. Spencer, P. A. Norreys, R. J. Clarke, R. Kodama, Y. Toyama, and M. Tampo, Appl. Phys. Lett. **80**, 2129 (2002).

[16]C. Courtois, R. Edwards, A. Compant La Fontaine, C. Aedy, S. Bazzoli, J. L. Bourgade, J. Gazave, J. M. Lagrange, O. Landoas, L. Le Dain, D. Mastrosimone, N. Pichoff, G. Pien, and C. Stoeckl, Phys. Plasmas **20**, 083114 (2013).

[17]J. Baggio, D. Raffestin, N. Blanchot, 40th EPS conference on Plasma Physics, O6.508 (2013).

[18]T. T. Liang, J. M. Bauer, J. C. Liu, and S. H. Rokni, Health Physics, 115, 687 (2018).

[19]R. J. Clarke, D. Neely, R. D. Edwards, P. N. M. Wright, K. W. D. Ledingham, R. Heathcote, P. McKenna, C. N. Danson, P A Brummitt, J. L. Collier, .P EHatton, S. J. Hawkes, C. Hernandez-Gomez, P. Holligan, M. H. R. Hutchinson, A. K. Kidd, W. J. Lester, D. R. Neville, P. A. Norreys, D. A. Pepler, T. B. Winstone, R. W. W. Wyatt and B. E. Wyborn, J. Radiol. Prot. **26**, 277 (2006).

[20]A. Compant La Fontaine, C. Courtois, F. Gobet, F. Hannachi, J. R. Marques, M. Tarisien, M. Versteegen and T. Bonnet, Phys. Plasmas **26**, 113109 (2019).

[21]C. Courtois, A. Compant La Fontaine, O. Landoas, G. Lidove, V. Méot, P. Morel, R. Nuter, E. Lefebvre, A. Boscheron, J. Grenier, M.M. Aléonard, M. Gerbaux, F. Gobet, F. Hannachi, G. Malka, J.N. Scheurer, and M. Tarisien, Phys. Plasmas. **16**, 013105 (2009).

[22]R. Benattar, C. Popovics, and R. Sigel, Rev. Sci. Instrum. **50**, 1583 (1979).

[23]Tarisien, C. Plaisir, F. Gobet, F. Hannachi, M. M. Aléonard, and A. Rebii, Rev. Sci. Instrum. **82**, 023302 (2011).

[24]C. Courtois, R. Edwards, A. Compant La Fontaine, C. Aedy, M. Barbotin, S. Bazzoli, L. Biddle, D. Brebion, J.L. Bourgade, D. Drew, M. Fox, M. Gardner, J. Gazave, J.M. Lagrange, O. Landoas, L. Le Dain, E. Lefebvre, D. Mastrosimone, N. Pichoff, G. Pien, M. Ramsay, A. Simons, N. Sircombe, C. Stoeckl, and K. Thorp, Phys. Plasmas. **18**, 023101 (2011).

[25]C.D. Chen, P.K. Patel, D.S. Hey, A.J. Mackinnon, M.H. Key, K.U. Akli, T. Bartal, F.N. Beg, S. Chawla, H. Chen, R.R. Freeman, D.P. Higginson, A. Link, T.Y. Ma, A.G. MacPhee, R.B. Stephens, L.D. Van Woerkom, B. Westover, and M. Porkolab, Phys. Plasmas **16**, 082705 (2009).

[26]J. Howe, D. M. Chambers, C. Courtois, E. Förster, C. D. Gregory, I. M. Hall, O. Renner, N. C. Woolsey, Rev. Sci. Instrum **77**, 036105 (2006).

[27]J Galy, M Maucec, D J Hamilton, R Edwards and J Magill, New Journal of Physics **9**, 23 (2007).

[28]E. Lefebvre, N. Cochet, S. Fritzler, V. Malka, M. M. Al_eonard, J. F. Chemin, S. Darbon, L. Disdier, J. Faure, A. Fedotoff, O. Landoas, G. Malka, V. M_eot, P. Morel, M. Rabec Le Gloahec, A. Rouyer, C. Rubbelynck, V. Tikhonchuk, R. Wrobel, P. Audebert, and C. Rousseaux, Nucl. Fusion **43**, 629 (2003).

[29]H. M. Abhold and J. S. Hendricks, Los Alamos National Laboratory Report No. LA 13709-M, edited by J. F. Briesmeister, 2000.

[30]E. Lefebvre, S. Bernard, C. Esnault, P. Gauthier, A. Grisollet, P. Hoch, L. Jacquet, G. Kluth, S. Laffite, S. Liberatore, I. Marmajou, P.-E. Masson-Laborde, O. Morice and J.-L. Willienoll, Nucl. Fusion **59**, 032010 (2019).

[31]National Technical Information Service Document no. DE10150216 (J. D. Johnson, " The SESAME database," LANL Report No. LA-UR-94–1451 (1994).

[32]F. J. D. Serduke, E. Minguez, S. J. Davidson, and C. A. Iglesias, JQSRT **65**, 527 (2000).

[33]T. E. Tierney, J. A. Cobble, B. G. DeVolder, N. M. Hoffman, D. L. Tubbs, P. A. Bradley, S. R. Goldman, G. R. Magelssen, and D. L. Paisley, Proc. SPIE 6261, High-Power Laser Ablation VI, 626106 (2006).

[34]G. Huser, C. Courtois, M. C. Monteil, Phys. Plasmas 16, 032703 (2009).

[35]A. Compant La Fontaine, J. Phys. D : Appl. Phys. **47**, 325201 (2014).

[36]A. Compant La Fontaine, C. Courtois, E. Lefebvre, Phys. Plasmas **19**, 023104 (2012).

[37]O. Culfa, G. J. Tallents, A. K. Rossall, E. Wagenaars, C. P. Ridgers, C. D. Murphy, R. J. Dance, R. J. Gray, P. McKenna, C. D. R. Brown, S. F. James, D. J. Hoarty, N. Booth, A. P. L. Robinson, K. L. Lancaster, S. A. Pikuz, A. Ya. Faenov, T. Kampfer, K. S. Schulze, I. Uschmann, and N. C. Woolsey, Phys. Rev. E **93**, 043201 (2016).

[38]A. Compant La Fontaine, Phys. Plasmas **25**, 043301 (2018).

[39]See http://physics.nist.gov/PhysRefData/XrayMassCoef for "NIST Database."

[40]A. Compant La Fontaine, C. Courtois, E. Lefebvre, J. L. Bourgade, O. Landoas, K. Thorp, and C. Stoeckl, Phys. Plasmas **20**, 123111 (2013).

[41]L. C. Jarrott, A. J. Kemp, L. Divol, D. Mariscal, B. Westover, C. McGuffey, F. N. Beg, M. Suggit, C. Chen, D. Hey, B. Maddox, J. Hawreliak, H.-S. Park, B. Remington, M. S. Wei, and A. MacPhee, Phys. Plasmas **21**, 031211 (2014).

[42]T. Yabuuchi, B. S. Paradkar, M. S. Wei, J. A. King, F. N. Beg, R. B. Stephens,N. Nakanii, M. Hatakeyama, H. Habara, K. Mima, K. A. Tanaka, and J. T. Larsen, Phys. Plasmas **17**, 060704 (2010).

FIGURES CAPTIONS

FIG. 1. (a) ELFIE experimental set-up, (b) schemes of the laser pulses and (c) scheme of the target.

FIG.2 Signal obtained with the x-ray spectrometer (a) for shots performed with different gaps g and delays δt. (b) and (c) X-ray spectrum inferred from both the activation measurement at 12° and the hard x-ray spectrometer (thick lines) for g = 0 µm and g = 400 µm respectively. Corresponding cumulated dose (thin lines) for E_γ^{min} = 0.5 MeV. (d) Electron spectrum obtained for δt = 0.5 ns, with a PET foil only without Ta conversion target.

FIG. 3. X-ray dose normalized to the incident laser energy as a function of the delay δt for different gap values.

FIG. 4. Examples of interferogram obtained a) when the long pulse is not activated (g = 700 µm), b) when the long pulse is activated (g = 700) µm and a delay of δt = 1 ns.

FIG. 5. 2D cylindrical TROLL simulations of the electron density n_e at t = - 0.6 ns (a) in the case of g = 400 µm (top part of the image) and gap = 0 µm (low part of the image) and at t = + 0.5 ns (b) and t = + 1.8 ns (c) for 700 µm gap.

FIG. 6. On-axis (r = 0) electron density n_e as a function of time for a 700 µm gap.

FIG. 7. (a) On-axis simulated (gray region) and measured (black dotted line) electron density at t = + 2 ns for gap = 0 µm. b) and c) Simulated (gray region) and measured (symbols) characteristic length L_p as a function of time for g = 0 µm and g = 400 µm respectively. The upper and lower

bounds of the gray region are associated to ±10% variation on the long pulse energy and foil thickness during TROLL simulations.

FIG. 8. (a) Evolution of the short pulse laser waist w(z) using the Gaussian beam equation in vacuum (gray solid line) and a modified version of this equation that takes into account laser self-focusing effect in the plasma (gray dotted line) from CALDER simulation. TROLL simulated electron density profile as a function of position z for the case g = 0 and at δt = 0 ns (black solid line). (b) and (c) Parameters W_{SF}/W_0 and Z_{foc} as a function a time determined from CALDER PIC simulations (black symbols) and used in the x-ray dose model for g = 0 from TROLL hydrodynamic simulations (gray solid line).

FIG. 9.: Measured (symbols) and simulated (solid line) normalized x-ray dose as a function of the gap size.

FIG. 10. (a) X-ray dose normalized to the laser energy (gap = 0) as a function of plasma scale length L_p (lower horizontal axis) and time (upper horizontal axis) obtained from CALDER-MCNP simulation (hollow circles), the dose model (gray region) and from the ELFIE experiment (black triangles). The upper and lower bounds of the gray region are associated to ±10% variation on the long pulse energy and foil thickness during TROLL simulations. Results from the model coupled to TROLL simulation showing (b) the on-axis plasma density, (c) the laser beam diameter, and (d) the electron energy as a function of the position z and time for gap = 0.

FIG. 11. (a) X-ray dose normalized to the laser energy (g = 400 μm) as a function of time, obtained from the dose model with (gray region) and without (black dashed curve) gap effect, and from the ELFIE experiment (black triangles). The upper and lower bounds of the gray region are associated to ±10% variation on the long pulse energy and foil thickness during TROLL simulations. Results from

the model coupled to TROLL simulations showing (b) the on-axis plasma density, (c) the laser beam diameter and (d) the electron energy as a function of the position z and time in the case of g = 400 µm.

FIG. 12. (a) X-ray dose normalized to the laser energy (g = 100 µm) as a function of time, obtained from the dose model with (gray region) and without (black dashed curve) gap effect, and from the ELFIE experiment (black triangles). The upper and lower bounds of the gray region are associated to ±10% variation on the long pulse energy and foil thickness during TROLL simulations. Results from the model coupled to TROLL simulations showing (b) the on-axis plasma density, (c) the laser beam diameter and (d) the electron energy as a function of the position z and time in the case of g = 100 µm.

FIG. 13. Maximum normalized dose (a) and time at which it is produced (b) as a function of the long pulse focal spot diameter ϕ_{lp} (at constant laser intensity), in the case of g = 400 µm.

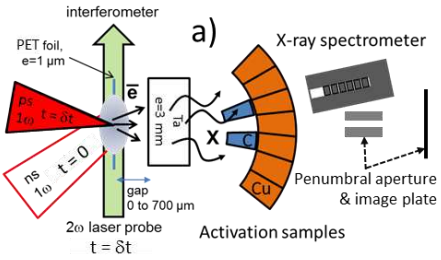

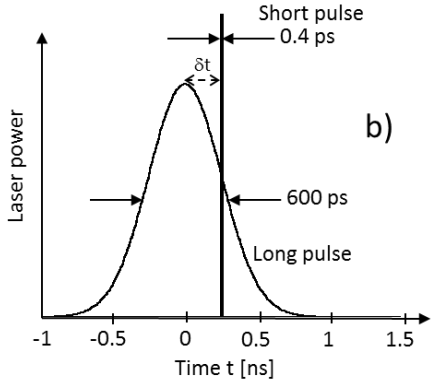

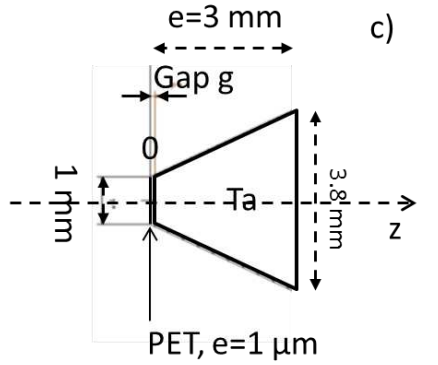

Fig. 1 Courtois

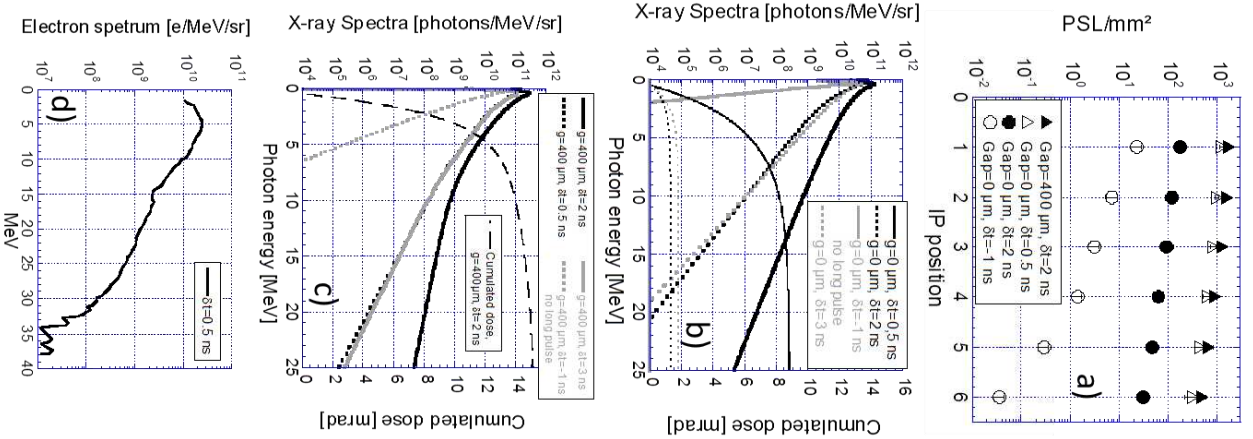

Fig. 2 Courtois

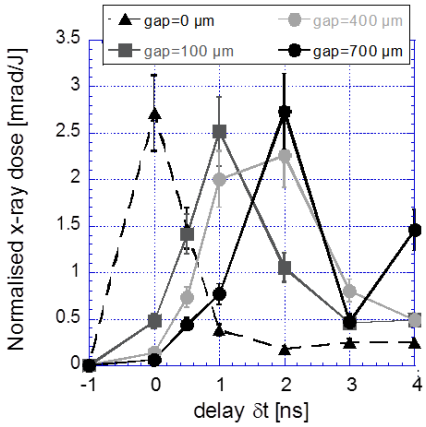

Fig. 3 Courtois

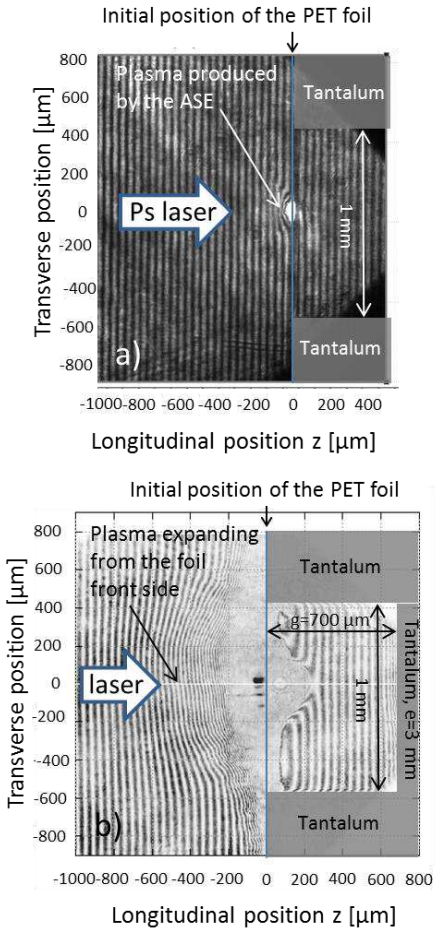

Fig. 4 Courtois

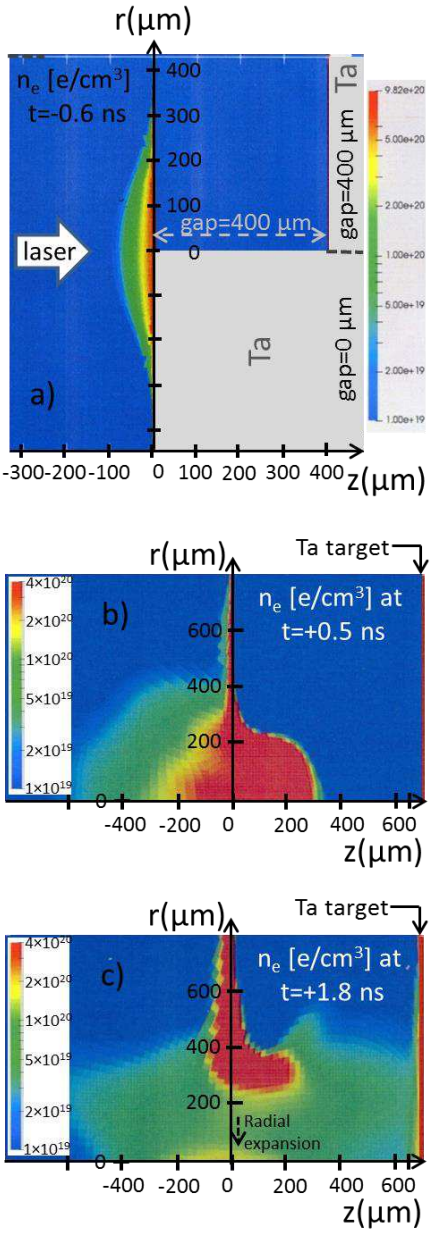

Fig. 5 Courtois

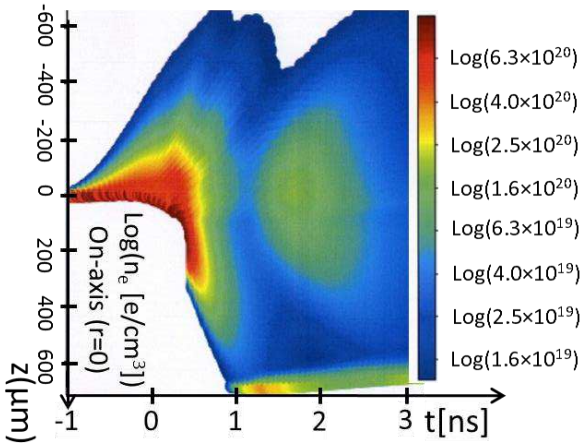

Fig. 6 Courtois

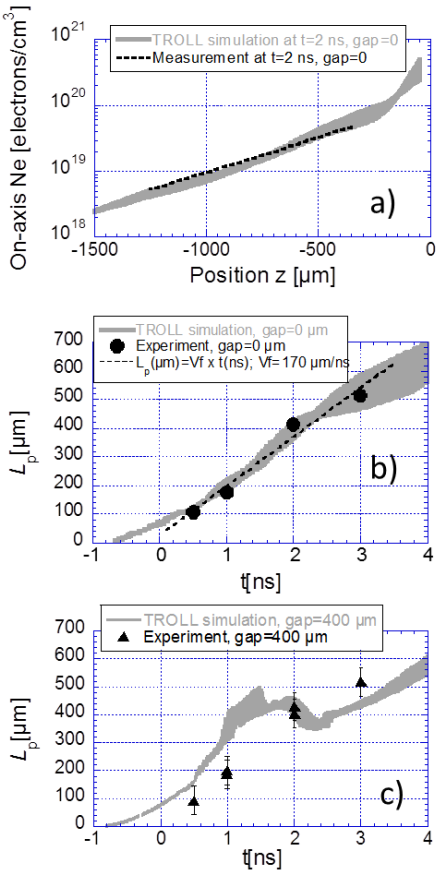

Fig. 7 Courtois

Fig. 8 Courtois

Fig. 9 Courtois

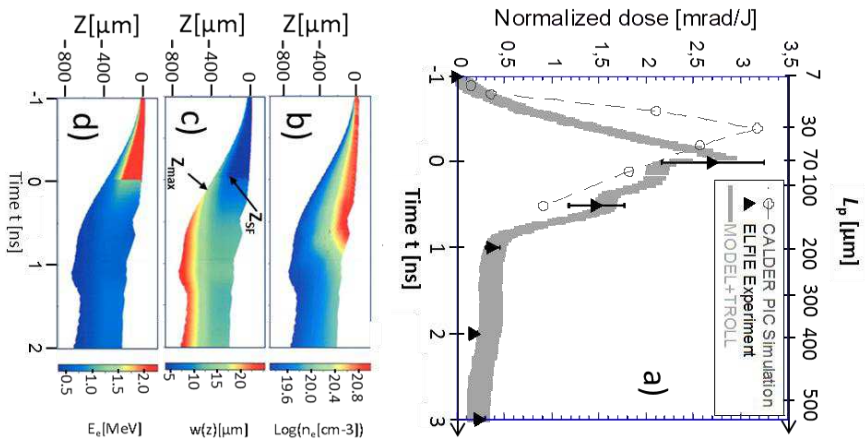

Fig. 10 Courtois

Fig. 11 Courtois

Fig. 12 Courtois

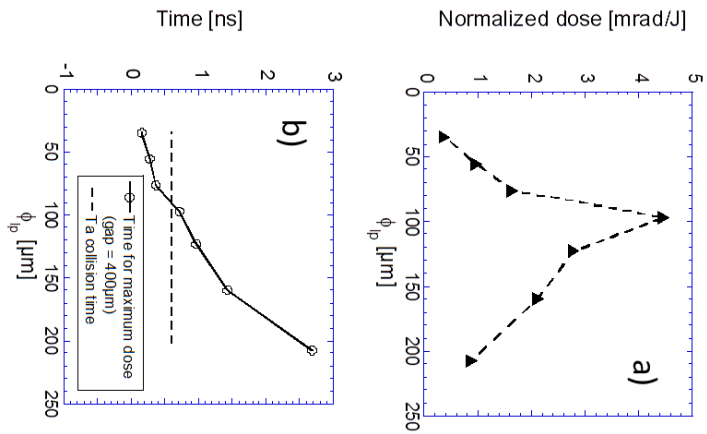

Fig. 13 Courtois

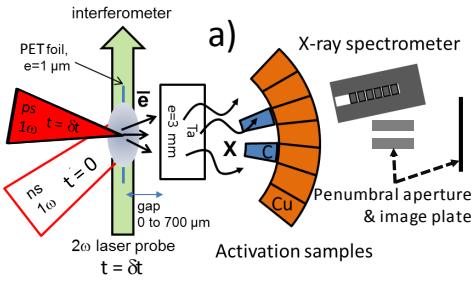

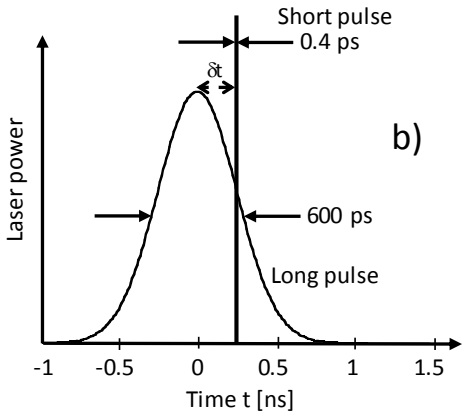

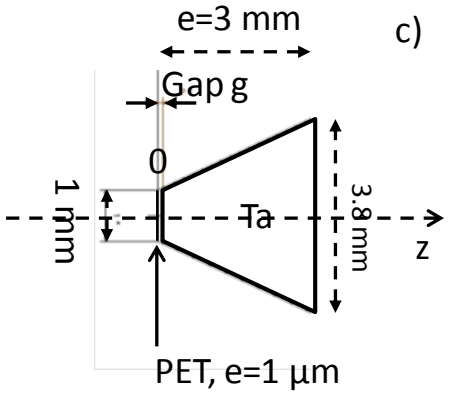

Fig. 1 courtois

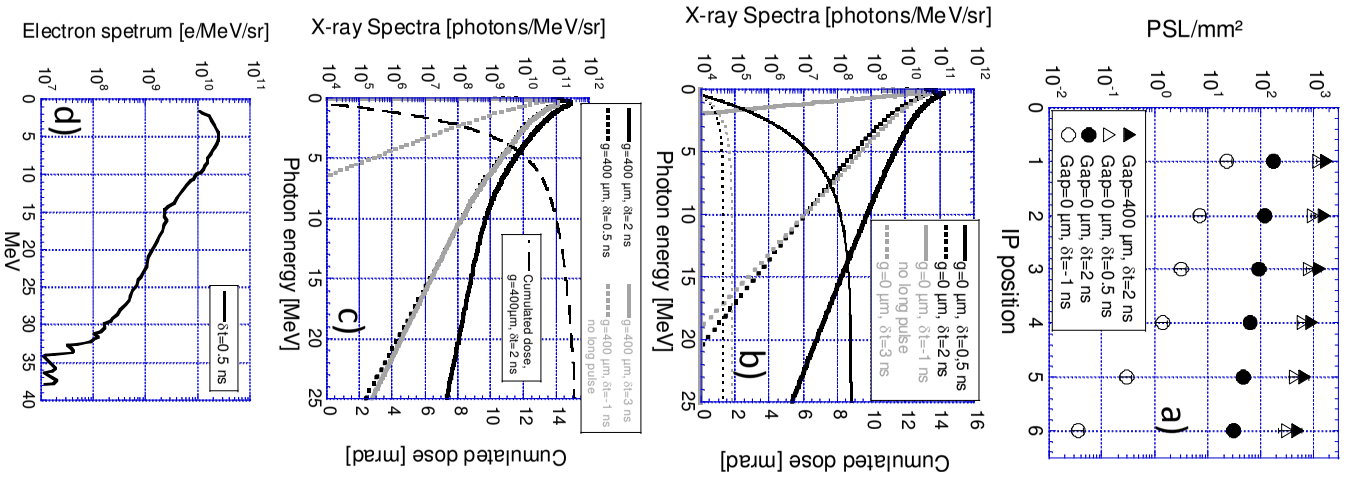

Fig. 2 courtois

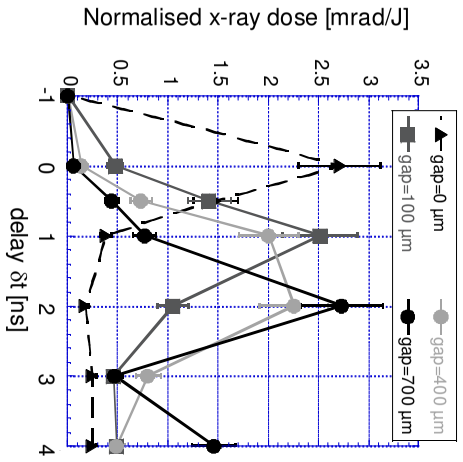

Fig. 3 courtois

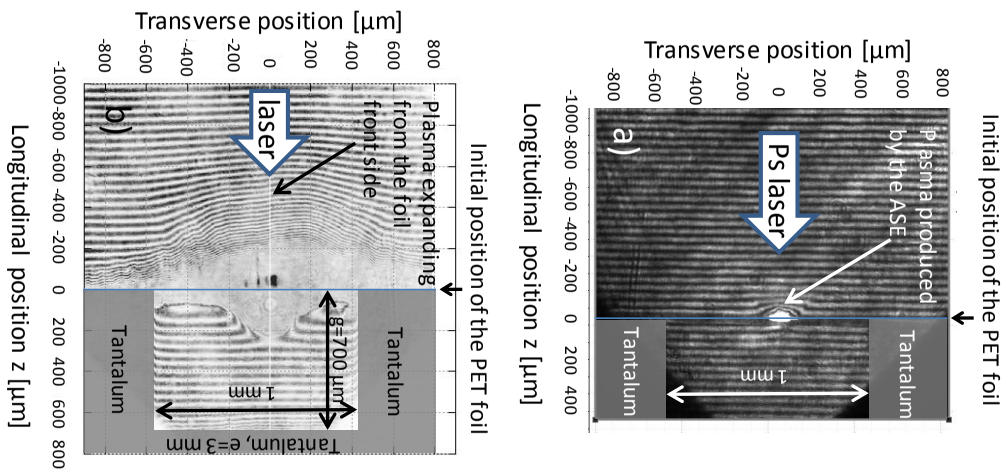

Fig. 4 courtois

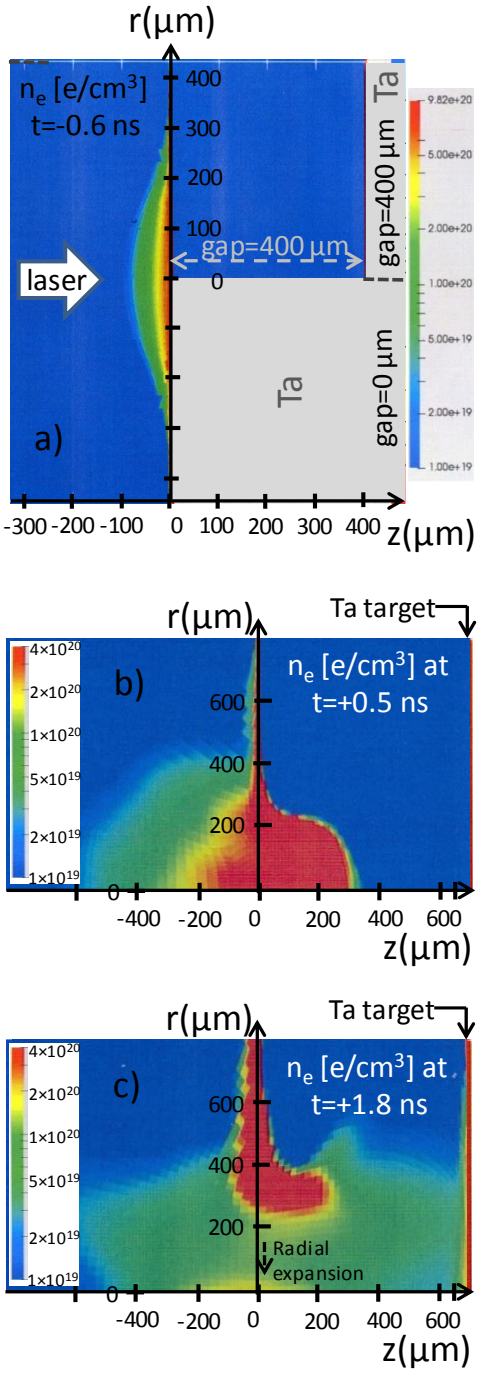

Fig. 5 courtois

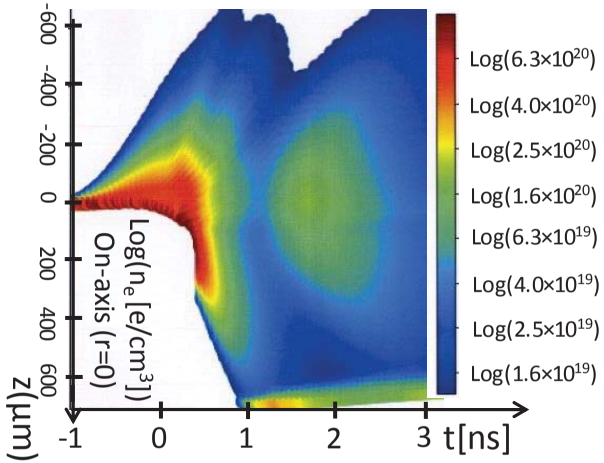

Fig. 6 courtois

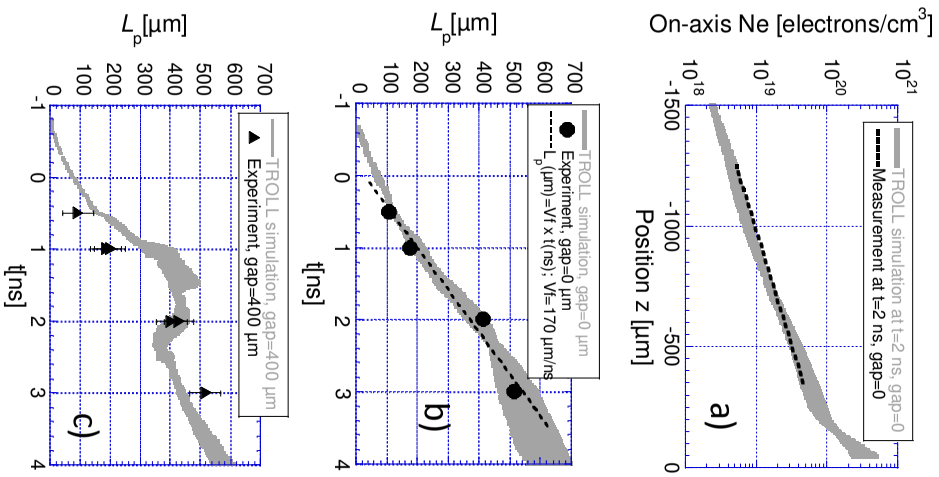

Fig. 7 courtois

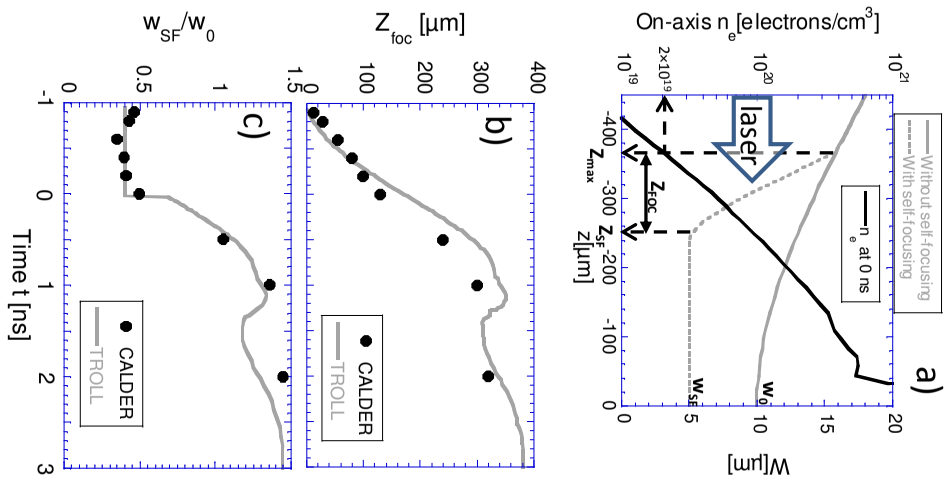

Fig. 8 courtois

Fig. 9 courtois

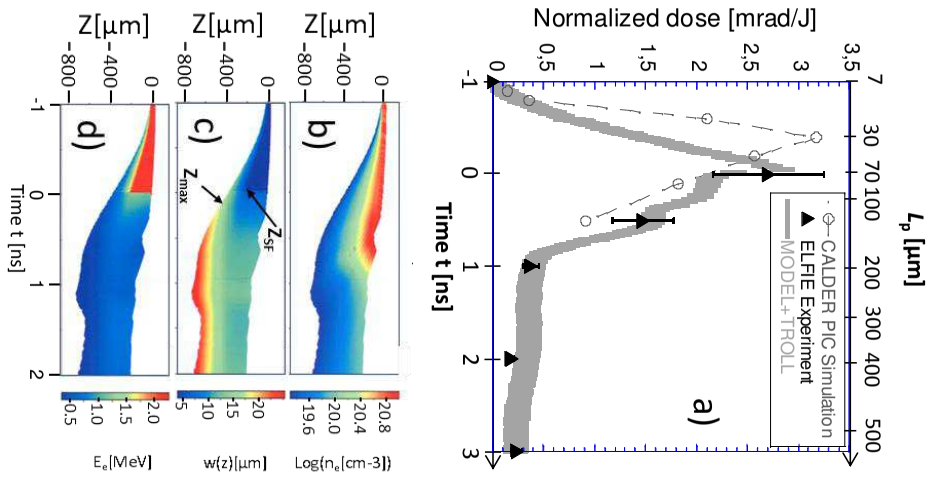

Fig. 10 courtois

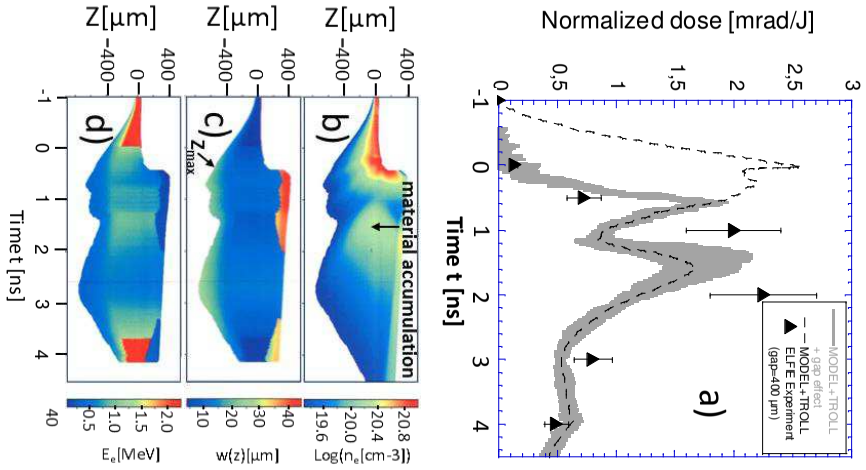

Fig. 11 courtois

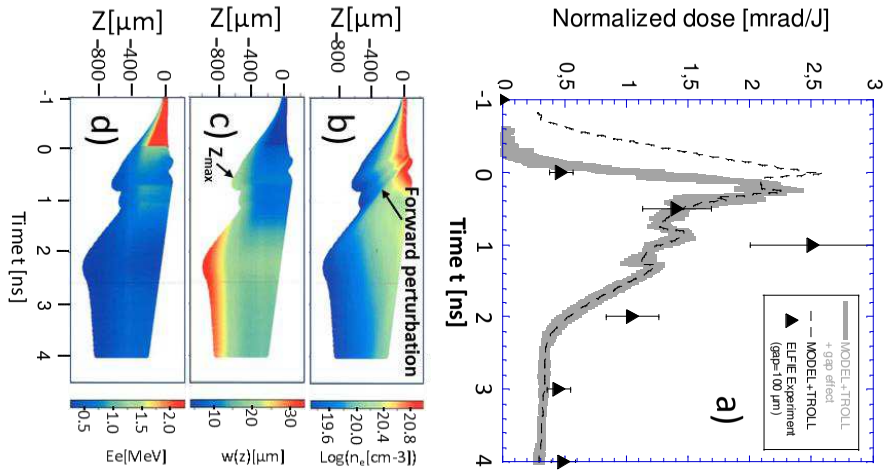

Fig. 12 courtois

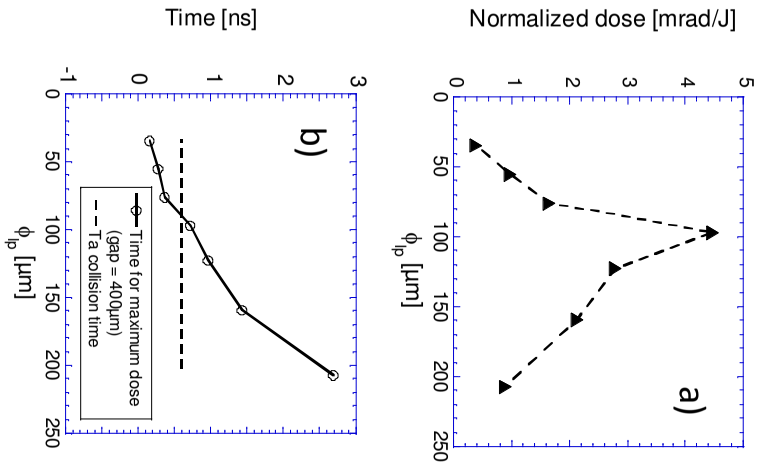

Fig. 13 courtois